J(Si,H) Coupling Constants of Activated Si-H Bonds

Journal:	*Journal of the American Chemical Society*
Manuscript ID	Draft
Manuscript Type:	Article
Date Submitted by the Author:	n/a
Complete List of Authors:	Meixner, Petra; Universität Augsburg, Institut für Physik Batke, Kilian; Universität Augsburg, Institut für Physik Fischer, Andreas; Universität Augsburg, Institut für Physik Schmitz, Dominik; Universität Augsburg, Institut für Physik Eickerling, Georg; Universität Augsburg, Institut für Physik Kalter, Marcel; Universität Augsburg, Institut für Physik Ruhland, K; Universität Augsburg, Institut für Physik Eichele, Klaus; Universitaet Tuebingen, Barquera-Lozada, Jose; Universidad Nacional Autonoma de Mexico, Instituto de Quimica Casati, Nicola; Paul Scherrer Institute, Montisci, Fabio; University of Berne, Department of Chemistry & Biochemistry Macchi, Piero; University of Bern, Chemistry and Biochemistry Scherer, Wolfgang; Universitaet Augsburg, Lehrstuhl fuer Chemische Physik

J(Si,H) Coupling Constants of Activated Si-H Bonds

Petra Meixner,[†] Kilian Batke,[†] Andreas Fischer,[†] Dominik Schmitz,[†] Georg Eickerling,[†] Marcel Kalter,[†] Klaus Ruhland,[†] Klaus Eichele[‡], José E. Barquera-Lozada,[§] Nicola P. M. Casati,[⊥] Fabio Montisci,[⊥,¶] Piero Macchi,[¶] Wolfgang Scherer*[†]

[†]Institut für Physik, Universität Augsburg, Universitätsstraße 1, 86135 Augsburg, Germany

[‡]Institut für Anorganische Chemie, Universität Tübingen, Auf der Morgenstelle 18, 72076 Tübingen, Germany

[§]Instituto de Química, Universidad Nacional Autónoma de México, Ciudad Universitaria, 04510 Mexico

[⊥]Paul Scherrer Institut, WLGA/229, 5232 Villigen PSI, Switzerland

[¶]Department of Chemistry & Biochemistry, University of Berne, Freiestrasse 3, 3012 Berne, Switzerland

KEYWORDS: nonclassical silane complexes • coupling constants • NMR spectroscopy • charge density • high pressure

Abstract: We outline in this combined experimental and theoretical NMR study that sign and magnitude of *J*(Si,H) coupling constants provide reliable indicators to evaluate the extent of the oxidative addition of Si-H bonds in hydrosilane complexes. In combination with experimental electron density studies and MO analyses a simple structure-property relationship emerges: *positive J*(Si,H) coupling constants are observed in cases where *M*→*L* π-back donation (*M* = transition metal; *L* = hydrosilane ligand) dominates. The corresponding complexes are located close to the terminus of the respective oxidative addition trajectory. In contrast *negative J*(Si,H) values signal the predominance of significant covalent Si-H interactions and the according complexes reside at an earlier stage of the oxidative addition reaction pathway. Hence, in non-classical hydrosilane complexes such as $Cp_2Ti(PMe_3)(HSiMe_{3-n}Cl_n)$ (with *n*=1-3) the sign of *J*(Si,H) changes from *minus* to *plus* with increasing number of chloro substituents *n* and maps the rising degree of oxidative addition. Accordingly, the sign and magnitude of *J*(Si,H) coupling constants can be employed to identify and characterize non-classical hydrosilane species also in solution. These NMR studies might therefore help to reveal the salient control parameters of the Si-H bond activation process in transition-metal hydrosilane complexes which represent key intermediates for numerous metal-catalyzed Si-H bond activation processes. Furthermore, experimental high-resolution and high-pressure X-ray diffraction studies were undertaken to explore the close relationship between the topology of the electron density displayed by the η^2(Si-H)*M* units and their respective *J*(Si,H) couplings.

INTRODUCTION

It is often assumed that the reaction between an Si-H moiety of hydrosilanes $SiHR_3$ (*R* = alkyl, aryl, halogen) and organometallic fragments ML_n (*M* = transition metal; *L* = ligand) yields silyl hydride complexes as oxidative addition products.[1] Such *classical* silyl hydride species are characterized by the presence of two covalent *M*-Si and *M*-H bonds and the lack of any residual Si···H interaction. However, in many cases a wide spectrum of nonclassical bonding scenarios can be observed instead (Figure 1). These nonclassical hydrosilane complexes can be considered as arrested intermediates along the oxidative addition pathway.[1] This is illustrated in Figure 1 by selected benchmark systems, where the σ-complex $Cr(CO)_5SiH_2Ph_2$ (**1**)[2a] and the classical silyl hydride $Fe(CO)_4H(SiCl_3)$ (**7**)[2b] represent starting point and terminus of this process. The propagation along the oxidative addition pathway can then be considered as a continuum of electronic structures.[3] Accordingly, the d^6 manganese complex $(CH_3)CpMn(CO)_2(HSiHPh_2)$ (**2**) can be characterized as a σ-complex but shows already an enhanced *M*···Si interaction relative to **1**.[3a,3h,4a] Hence, **1** and **2** can be distinguished by their η^1/η^2 (Si-H)*M* coordination modes, respectively.[1c] The *M*···Si interaction increases further in $(CH_3)CpMn(CO)_2(HSiFPh_2)$ (**3**)[4a,b] which displays an electron withdrawing substituent at the silicon atom of the hydrosilane ligand yielding an *a*symmetric *o*xidative *a*ddition *p*roduct (ASOAP).[1c,3f] A similar scenario can be also observed in case of the early transition metal hydrosilane complexes such as the d^2-titanium complexes $Cp_2Ti(PMe_3)(HSiHPh_2)$ (**4**)[4c] and $Cp_2Ti(PMe_3)(HSiHPhCl)$ (**5**)[5]. The extent of Si-H bond activation increases only insignificantly from **3-5**, however, the *J*(Si,H) spin-spin couplings change drastically from -52 Hz to +23 Hz. It will be therefore one aim of this report to explain these puzzling NMR features which we have already used at this stage to group the ASOAPs **3-5** along the reaction coordinate of the oxidative addition path. Finally, we introduce the d^8 Ni-complex $Ni(iPr_2Im)_2(HSiMePh_2)$ (**6**)[4d] (*i*Pr_2Im=1,3-

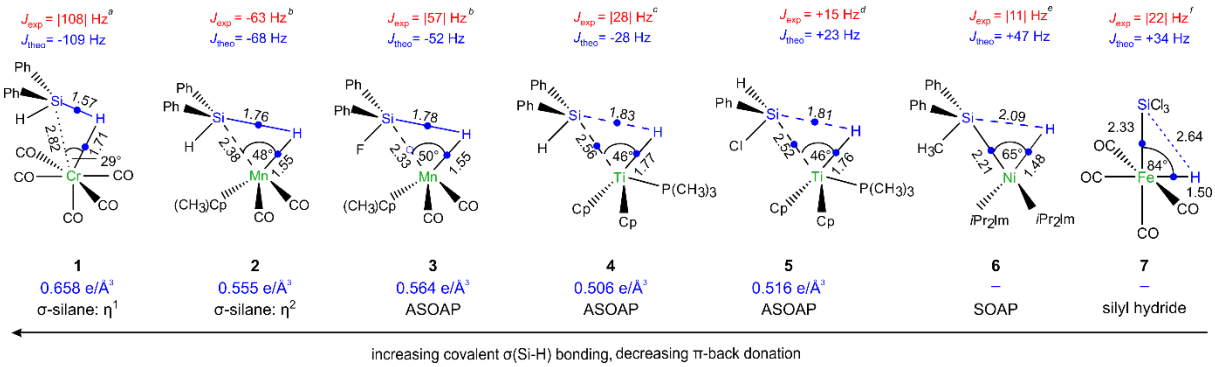

Figure 1. Calculated structural parameters of selected (*i*) σ-silane complexes, (*ii*) asymmetric and symmetric oxidation addition products (ASOAP and SOAP, respectively), and (*iii*) classical silyl hydride complexes (distances in Å). Experimental and theoretical *J*(Si,H) spin-spin coupling constants are specified in red and blue color, respectively. The calculated electron density accumulation, $\rho(\mathbf{r})$, at Si-H bond critical points (BCPs) in **1-5** is specified below each structure and the BCPs are shown as filled blue circles. Note that the *M*-Si BCP is missing in the η^1/η^2 σ-silane complexes **1** and **2** while the SOAP and silyl hydride complexes **6** and **7**, respectively, are characterized by lacking Si-H BCPs. In contrast, the non-classical complexes **4-5** display all the expected and characteristic critical points of a three-membered metallacycle. In case of complex **3**, the *M*-Si BCP is present only in the experimental $\rho(\mathbf{r})$, as symbolized by an open blue circle. [a] ref 2a, [b] this work, [c] ref 4c, [d] ref 5, [e] ref 3i,4d, [f] ref 2b.

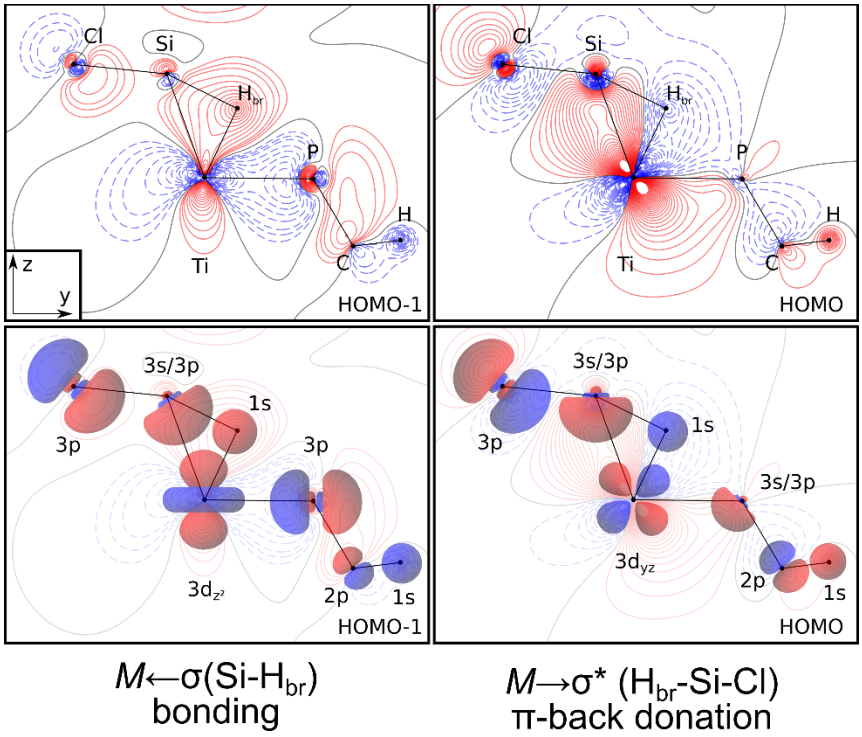

Figure 2. Top: Molecular orbital (MO) plot of the *M*←σ(Si-H_{br}) (HOMO-1) and the *M*→σ*(H_{br}-Si-Cl) (HOMO) of $Cp_2Ti(PMe_3)$(HSiHPhCl) **5**, respectively. These MOs represent exemplary the σ donation and π back donation components which mainly control the nature and strength of the interaction between hydrosilane ligands and transition metal fragments. Below: Schematic envelope drawings highlighting predominant contribution of valence atomic orbitals to HOMO-1 and HOMO of **5**.

diisopropylimidazolin-2-ylidene) in Figure 1 as a benchmark for a *s*ymmetric *o*xidative *a*ddition *p*roduct (SOAP).[3i] This complex differs from a classical silyl hydride characterized by 2-electron, 2-center (2e/2c) M-Si and M-H bonds by the presence of a residual Si···H interaction. Note that we refer in Figure 1 to theoretical values based on the ZORA-Hamiltonian and the PBEo/TZ2P level of approximation. These values are unbiased by solvation or crystal packing effects and allow a direct comparison of salient benchmark systems also in cases where an experimental determination of structural parameters or NMR properties (i.e. the sign of the *J* couplings) was hindered by the chemical instability of the respective samples (see Experimental and Computational Section). If not specified otherwise we will also refer to values calculated at the same level of approximation in the following part.

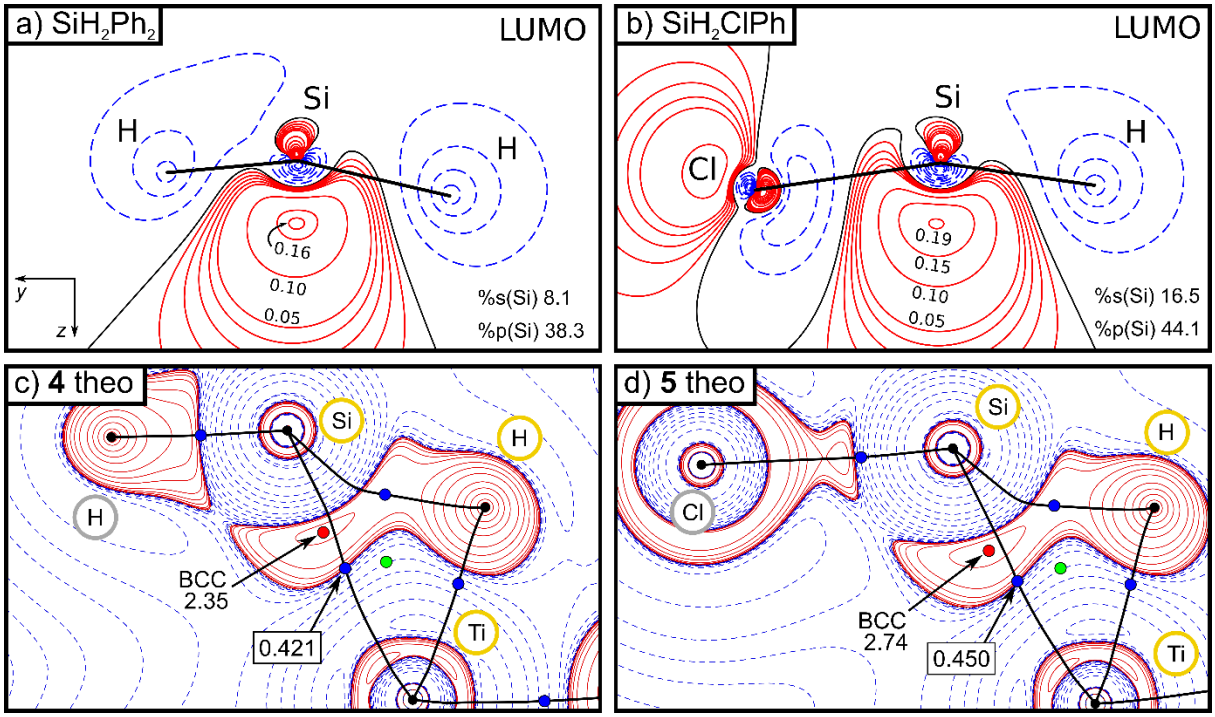

Figure 3. Plot of the frontier orbitals $\sigma^*(H_{br}\text{-Si-}X)$ (LUMO) of the silane ligands a) SiH_2Ph_2 and b) SiH_2ClPh with constrained structural parameters adopted from the parent complexes **4** and **5**, respectively. Contour levels are specified in atomic units and the percentage %s and %p character of the silicon atom refers to SFO gross populations of symmetrized fragment (valence) orbitals (SFO). c,d) Theoretical $L(\mathbf{r}) = -\nabla^2\rho(\mathbf{r})$ maps of hydrosilane complexes **4** and **5** in the plane defined by *M*, Si and H_{br}; positive (red, solid) and negative (blue, dashed) $L(\mathbf{r})$ contour lines were drawn at $\pm 2.0^{\times}10^{n}$, $\pm 4.0^{\times}10^{n}$, $\pm 8.0^{\times}10^{n}$ e/Å^5 with $n = \pm 2, \pm 1, 0$. Bond paths are displayed as black solid lines. Bond critical points and ring critical points are drawn as blue and green filled circles, respectively. The bonded charge concentration (BCC) in the valence shell of charge concentration at silicon of **4** and **5** is specified in e/Å^5 and marked by a red spot and the values of the Ti-Si bond critical points are denoted in e/Å^3.

The continuum of electronic structures in Figure 1 can be explained by a unifying bonding concept[1c,6] based on an extended Dewar-Chatt-Duncanson (DCD) model[7]. In this model σ-hydrosilane complexes are characterized by their predominant $M\leftarrow\sigma(\text{Si-H}_{br})$ donation while *the propagation along the oxidative addition pathway is triggered by the increasing extent of the* $M\rightarrow\sigma^*(H_{br}\text{-Si-}X_t)$ *back donation* (Figure 2). In this bonding model X_t represents a silicon substituent located inside the $\eta^2(H_{br}\text{-Si})M$ plane in *trans*-orientation to the bridging hydrogen atom (H_{br}). The individual orbital interactions can be analyzed by defining a local coordinate system where the metal atom is located at the origin and the $\eta^2(H_{br}\text{-Si})M$ entity defines the *y*,*z* plane with the *z*-axis pointing to the midpoint of the H_{br}-Si bond.[8] The $M\rightarrow\sigma^*(H_{br}\text{-Si-}X_t)$ back donation can then be interpreted as the interaction between a d_{yz} orbital of the metal fragment ML_x (HOMO-*n*) and the antibonding $\sigma^*(H_{br}\text{–Si–}X_t)$ frontier orbital (LUMO) of the silane ligand. Hence, the oxidative addition reaction coordinate is mainly controlled by the electronic influence of the X_t-substituent: the higher the electron-withdrawing character of X_t, the larger the silicon character of the $\sigma^*(H_{br}\text{–Si–}X_t)$ frontier orbital (Figure 3a,b) and the shorter the corresponding *M*-Si bond.[3h,3i] A more detailed inspection (Figure 3a,b) shows, that these trends emerge directly from the chemical nature of free hydrosilane ligands. Direct comparison of the $\sigma^*(H_{br}\text{–Si–}X_t)$ frontier orbitals (LUMOs) of the SiH_2Ph_2 and SiH_2ClPh reveals all salient electronic effects which are inherently induced by the presence of an electronegative substituent at the silicon atom: (*i*) the silicon character *increases*,[9a] (*ii*) the silicon atoms gains a *larger s-character*[9b] and (*iii*) the frontier orbital contracts.[9c] As a consequence the sp^x hybridized lobe at silicon becomes more strongly polarized and contracted in *z*-direction in case of SiH_2ClPh compared with SiH_2Ph_2. This polarization/contraction effect controls the strength of the $M\rightarrow\sigma^*(H_{br}\text{-Si-Cl})$ back-donation and causes a stronger M-Si bond in **5** (Ti–Si = 2.52 Å) compared with **4** (Ti–Si = 2.56 Å). The polarization effect is also revealed by an increasing bonded charge concentration (BCC) in the valence shell of the silicon atom close to the *M*-Si bond path (Figure 3c,d). This BCC increases from $L(\mathbf{r}) = -\nabla^2\rho(\mathbf{r}) = 2.35$ e/Å^5 in **4** to $L(\mathbf{r}) = 2.74$ e/Å^5 in **5**. Also the *M*-Si bond critical points follow this trend and increase from 0.421 e/Å^3 in **4** to 0.450 e/Å^3 in **5**.

Also the Mn-Si bond lengths in the manganese complexes **2** (Si-Mn = 2.38 Å) and **3** (Si-Mn = 2.33 Å) follow this trend. Introduction of additional electron-withdrawing substituents at the silicon atom clearly enhances the *M*-Si bond strength. This electronic effect was experimentally observed by Schubert and coworkers already in 1986 by a combined X-ray and neutron diffraction study of the d^6 complexes **2** and **3**.[3a,4a,4b] Also the first theoretical studies by Fan et al.[3k] and Lin[3d] were in line with these findings and also predicted a continuous decrease of the *M*-Si bond lengths with increasing number of chlorine substituents in case of early transition metal hydrosilane complexes. This was experimentally

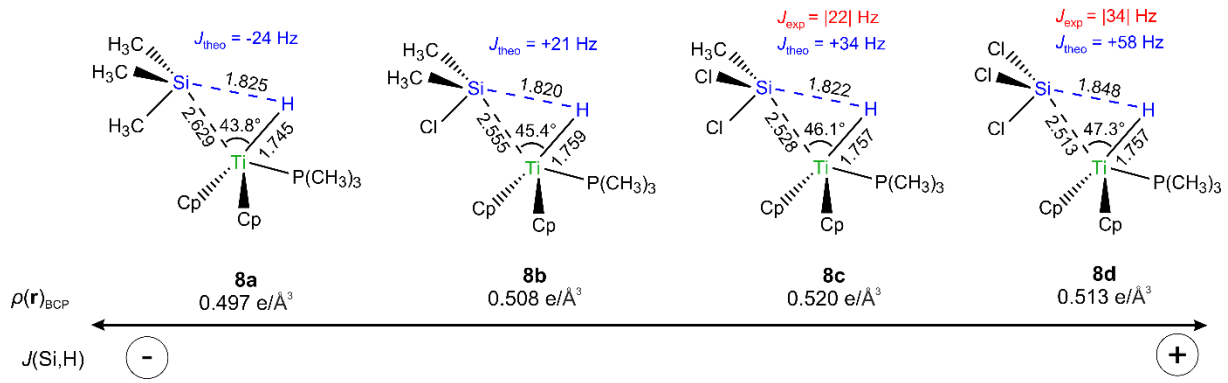

Figure 4. Salient structural parameters of nonclassical silyl hydride complexes **8a-8d**. Experimental and theoretical coupling constants are specified in red and blue color, respectively. Bond distances are specified in Å. Experimental *J*(Si,H) couplings of **8c** and **8d** were taken from ref. 10a.

Scheme 1. Nonclassical hydrosilane complexes 9a-d and 10a-e.

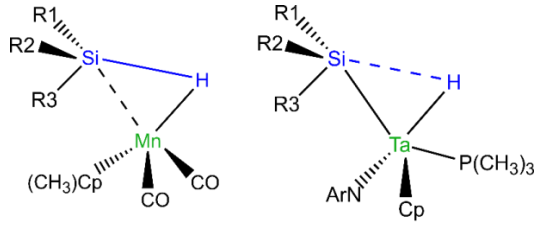

9a-d 10a-e

a: R1=R2=R3 = Me; b: R1=R2= Me, R3=Cl; c: R1=Me, R2=R3=Cl; d: R1=R2=R3=Cl; e: R1=H, R2 = Ph, R3=Me.

confirmed by Dubberly and Nikonov et al. in case of a series of d² complexes $Cp_2Ti(PMe_3)(HSiMe_{3-n}Cl_n)$ **8a-8d**[10a] for **8c** and **8d** (Figure 4) and $Cp(ArN)Ta(PMe_3)(H)(SiMe_{3-n}Cl_n)$ **10a-10d** (ArN = 2,6-$C_6H_3iPr_2$, *n* = 0-3; Scheme 1).[10b]

Also the origin of the acute and rather invariant ∠Si,*M*,H angle of 46-65° in the nonclassical silane complexes **2-6** (Figure 1) can be understood in terms of competing $M\leftarrow\sigma(H_{br}\text{-Si})$ donation and $M\rightarrow\sigma^*(H_{br}\text{-Si-}X_t)$ back donation processes.[3i] Hence, the $M\leftarrow\sigma(H_{br}\text{-Si})$ bonding orbital in Figure 2 displays mainly $M(d_{z^2})$ and H(1s) character and optimal orbital overlap is expected for acute ∠Si,*M*,H angles. In contrast, a ∠Si,*M*,H angle of 90° optimizes the $M(d_{yz})\rightarrow\ \sigma^*(X\text{–Si–H})$ back-donation. Hence, the acute ∠Si,*M*,H angles of nonclassical silane complexes (46-65° in **2-6**) appear to reflect the electronic compromise between these competing DCD components and hinder Si-H bond scission and the completion of the oxidative addition process. Accordingly, typical Si-H bond distances of nonclassical silane complexes are shorter than that of silyl hydride species such as **7** (Si-H = 2.64 Å; ∠Si,M,H = 84°) but significantly longer compared to those in σ-silane complexes such as **1** (1.57 Å, ∠Si,M,H = 29°) (Figure 1).

As a consequence of the electronically constrained ∠Si,*M*,H angles in nonclassical silane complexes, also the respective Si-H bond distances are rather invariant and cannot be employed as a measure of the stage of oxidative addition. Also the trans-influence of the electron-withdrawing silicon substituents on the Si-H bond strength is typically small and difficult to assess by structural studies. E.g. in the d⁶ Mn complexes **2** and **3**, the calculated Si-H bond distance increases slightly from 1.76 to 1.78 Å upon introduction of a chloro substituent at the silicon atom (Figure 1). Accordingly, the bond length difference is rather minute and within the typical range of estimated standard deviations in standard X-ray or neutron diffraction studies. Indeed, the Si-H bond distances in **2** and **3** where carefully determined by neutron diffraction and do not differ within their estimated standard deviations: $Si\text{-}H_{br}$ = 1.806(14) Å in **2**[3h] and $Si\text{-}H_{br}$ = 1.802(5) Å in **3**[4b]. Also analyses of the calculated Si-H bond lengths in the d² complexes $Cp_2Ti(PMe_3)(HSiMe_{3-n}Cl_n)$ **8a-8d** reveal only subtle changes in the Si-H bond lengths with regard to the halogen substitution degree *n* at the silicon atom (Figure 4). Furthermore, the geometrical trends observed for **8a-8d** appear to be non-systematic since a minimal Si-H bond distance is observed for **8b** (*n*=1) instead of **8d** displaying three electron withdrawing chloro substituents.[10a,5] However, a closer inspection of Figure 4 reveals that the Si-H bond distances of **8a-8d** in the three-membered Mn,Si,H metallacycle are mainly controlled by changes of the (*i*) *M*-Si bond length and of (*ii*) the ∠Si,*M*,H angle while (*iii*) the *M*-H bond distance in these ASOAPs changes only insignificantly upon variation of the silicon substituents. Hence, the larger degree of oxidative addition in **8b** vs. **8a** is not signaled by an elongated and more activated Si-H bond (Si-H = 1.825 Å and 1.820 Å in **8a** and **8b**, respectively). Apparently, the expected lengthening of the Si-H bond in **8b** vs **8a** as a geometrical consequence of the widened ∠Si,*M*,H angle in **8b** (45.4°) vs **8a** (43.8°) becomes overcompensated by the pronounced Ti-Si bond strengthening in **8b** (2.555 Å) vs **8a** (2.629 Å). $Si\text{-}H_{br}$ distances can therefore not be considered as sensitive measure of the degree of oxidative addition in ASOAP systems. Accordingly, it is the aim of this contribution to provide alternative measuring tools of the degree of oxidative addition in nonclassical hydrosilane complexes. In the next step we will therefore outline how even subtle electronic structure changes can be directly analyzed by charge density and NMR studies.

RESULTS AND DISCUSSION

Experimental and theoretical Charge Density Studies. In the electron density picture σ-silane complexes such as **1** are characterized by a pronounced density accumulation at the Si-H BCP (Figure 1). Due to the lack of a pronounced $M\rightarrow\sigma^*$(*X*-Si-H) back donation component, the *M*-Si BCP is lacking and **1** can be classified as η^1(Si-H) complex. Also the d^6 Mn complex **2** lacks a *M*-Si BCP.[3h] However, its *M*-Si interaction is already significant as witnessed by the short Mn-Si distance of 2.38 Å and the Si-H bond activation is already more developed in **2** vs **1** (Figure 1). This is clearly reflected in the corresponding densities at the corresponding BCPs (*M*-H: $\rho(\mathbf{r})$ = 0.470/0.796 e/Å^3 and Si-H: $\rho(\mathbf{r})$ = 0.658/0.555 e/Å^3 for **1** and **2**, respectively; see also the Supporting Information). As a consequence, **2** can be classified as a textbook example of a η^2(Si-H) species.[1c] In contrast, *nonclassical* silane complexes such as **3-5** and **8a-d** can be classified as asymmetric oxidative addition products since the *M*-Si BCPs (which are missing in **1** and **2**) have now been established (Figure 1; Figure 5a-f). This is the expected scenario for a three-membered η^2(Si-H_{br})*M* metallacycle where the bridging hydrido ligand (H_{br}) establishes covalent bonds simultaneously with the metal and the silicon atom. However, in contrast to the classical silyl hydride species, the *M*-Si BCP is topologically instable as signaled by the proximity of the *M*-Si BCP and the ring critical point (RCP). This is especially true for the borderline case **3** (Figure 5a,b) where the respective BCP is present in the experimental density map but lacking in the theoretical one. However, also in the experimental map of **3** the *M*-Si BCP and the RCP inside the η^2(Si-H_{br})*M* moiety nearly merge into a singularity in $\rho(\mathbf{r})$, a situation which hints for a *M*-Si bond catastrophe scenario.[11] Accordingly, the scenario depicted by the theoretical density map in Figure 5b shows the loss of the Mn-Si BCP as the final consequence of this bonding scenario. Note that the Si-H_{br} bond paths of the bridging η^2(Si-H_{br}) moiety in **3-5** and **8a-d** (see Figure 5a-f and the Supporting Information) are bent inwardly in line with the electron deficient nature of the η^2(Si-H_{br})*M* moieties. However, the density accumulation at the Si-H BCPs in **3-5** and **8a-d** (0.497–0.564 e/Å^3) is significantly higher than at the corresponding RCPs (0.387–0.424 e/Å^3) and only slightly smaller compared to the η^2(Si-H) complex **2** (0.555 e/Å^3). For corresponding experimental values, see Figure 5a,c,e and the Supporting Information.

Accordingly, the ASOAP complexes **3-5** and **8a-8d** are characterized by (*i*) covalent 2e/2c *M*-H bonds, (*ii*) significantly activated Si-H bonds and (*iii*) incipient *M*-Si bonds. This assumption is also supported by single-crystal diffraction studies of **8c** at variable pressure (Figure 6). Increasing the pressure stepwise from ambient conditions to 5.5(1) GPa results in a significant shortening of the Ti-Si bond distance by 0.04 Å (from 2.516(2) Å to 2.4756(8) Å) while the Si-H and Ti-H bonds did not change in the range of their estimated standard deviations. However, the compressibility of the dative Ti-P bond of the coordinating PMe_3 phosphine ligand by ca. 0.09 Å (Figure 6) is even larger than that of the Ti-Si bond in the same pressure range from 0 to 5.5 GPa. This is in line with our suggestion that the *M*-Si bond in **3-5** and **8a-8d** displays already covalent character - even though it is not yet fully developed. Apparently, the Ti-Si bond is clearly stronger than the dative Ti-P bond.

The d^8 nickel complex **6** represents our next benchmark system along this reaction coordinate since it is characterized by the simultaneous presence of a 2e/2c Ni-Si and a 2e/2c Ni-H bond. Indeed, the covalent Ni-Si bond of **6** (2.21Å) is even shorter than that of classical nickel(II) silyl complexes such as (dippe)Ni($SiCl_3$)Cl (dippe=1,2-bis(diisopropylphosphino) ethane; Ni-Si = 2.2390(8) Å) where electron-withdrawing substituents at the silicon atom enhance the strength of the Ni-Si bond.[12] Also the Ni-H bond length of 1.48 Å falls in the typical range of covalent nickel(II) hydrides such as [Cp*Ni(PEt_3)H] (Cp* = C_5Me_5) (Ni-H=1.46(3) Å).[13]

Accordingly, the nickel complex **6** represents a symmetric oxidative addition product (SOAP) characterized by covalent Ni-Si and Ni-H bonds and the lack of any Si-H BCP. In contrast to the classical silyl hydride **7**, however, the Si-H interaction in **6** is not completely broken[3i] as revealed by the analysis of the non-covalent interaction (NCI) Index (Figure 7).[14] In the NCI Index two scalar fields are employed to localize attractive and repulsive interaction domains: the electron density, $\rho(\mathbf{r})$, and the reduced density gradient (RDG, $s(\mathbf{r})$) as defined in formula (**1**) in atomic units.[14a]

$$s(\mathbf{r}) = \frac{1}{2(3\pi)^{1/3}}\frac{|\nabla\rho(\mathbf{r})|}{\rho(\mathbf{r})^{4/3}} \qquad (1)$$

Both scalar fields $s(\mathbf{r})$ and $\rho(\mathbf{r})$ are physical observable quantities and can be determined by high-resolution X-ray diffraction studies and subsequent modelling of the electron density distribution via multipolar refinements.[15] The combination of both scalar fields provides a partitioning of real space into covalent bonding domains (small *s* and large ρ values), non-covalent interaction zones (small *s* and small ρ values) and non-interacting density tails (large *s* and small ρ values).[14] Furthermore, the NCI indices rely also on the sign of the λ_2-eigenvalue of the density Hessian to classify interactions as bonding or non-bonding.[14] We note that the λ_2-eigenvalue at a specific point in space is one of the three solutions of the eigenvalue equation $(\nabla\nabla\rho(\mathbf{r}))\mathbf{u}_i = \lambda_i\mathbf{u}_i$. In a covalent bonding scenario, λ_2 represents the curvature of the electron density along the principal axis of curvature $\mathbf{u}_2$ (oriented perpendicular to the bond path). Accordingly, covalent bonding is signaled by a charge density accumulation in the plane perpendicular to the bond path (λ_2<0) and can be discriminated from non-bonding interactions (λ_2>0).

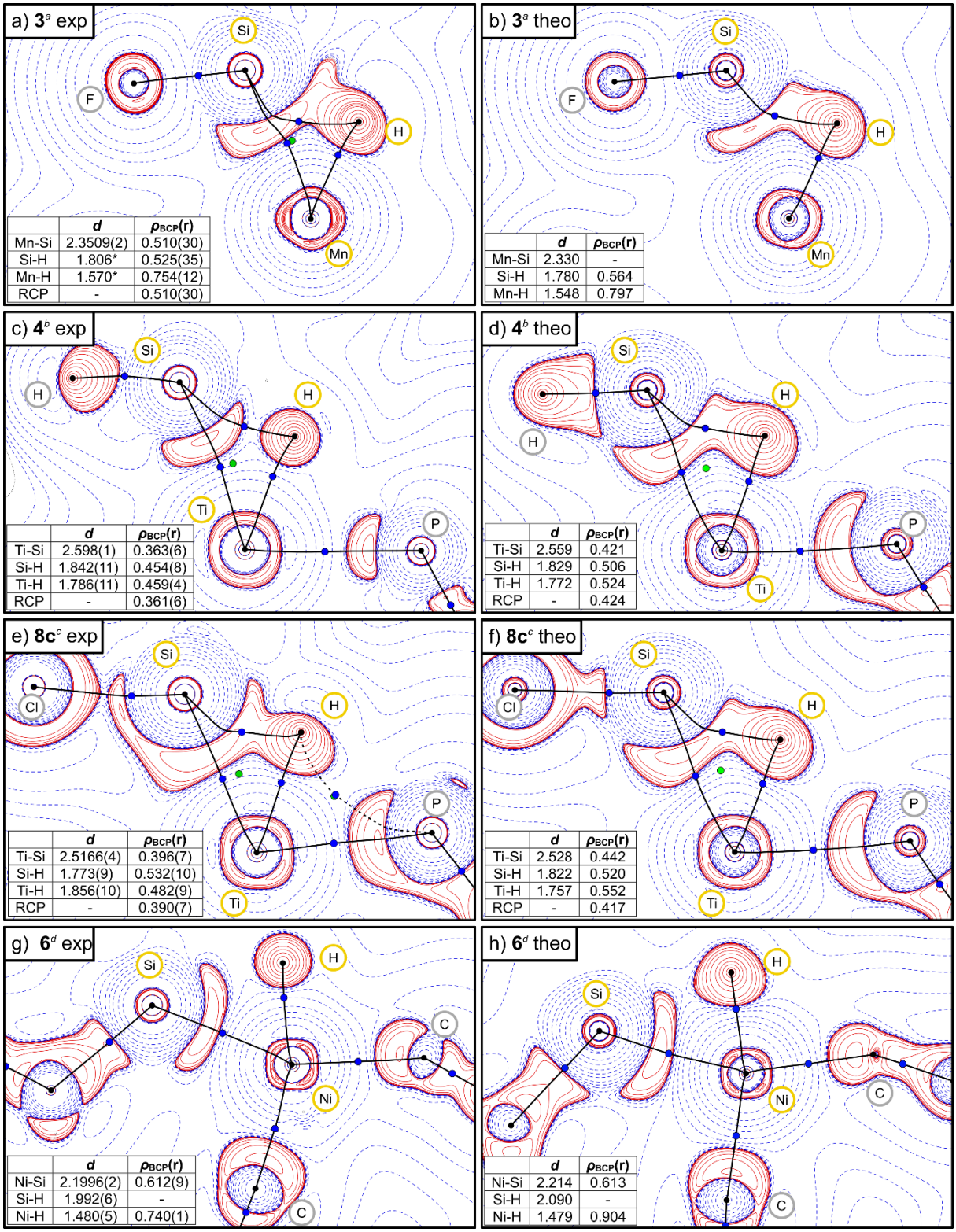

Figure 5. Experimental and theoretical $L(\mathbf{r}) = -\nabla^2\rho(\mathbf{r})$ maps of hydrosilane complexes **3**, **4**, **8c** and **6** in the plane defined by *M*, Si and H_{br}; positive (red, solid) and negative (blue, dashed) $L(\mathbf{r})$ contour lines were drawn at $\pm2.0^{\times}10^{n}$, $\pm4.0^{\times}10^{n}$, $\pm8.0^{\times}10^{n}$ e/Å^5 with n = ±2, ±1, 0. Extra lines were drawn at 11.5, 15, 500, 600 and 700 e/Å^5 in a); at 1000 and 1400 e/Å^5 in g) and h). The contour line at +400 e/Å^5 was removed in g) the contour line at +800 was removed in h). Bond paths are displayed as black solid lines. Bond critical points and ring critical points are drawn as blue and green filled circles, respectively. Salient bond distances and $\rho(\mathbf{r}_c)$ values at salient BCPs are given in the insets in [Å] and [e/Å^3], respectively. See the Supporting Information and Experimental Part for further details. [a] ref 3f, [b] ref 6, [c] this work, [d] ref 3i.

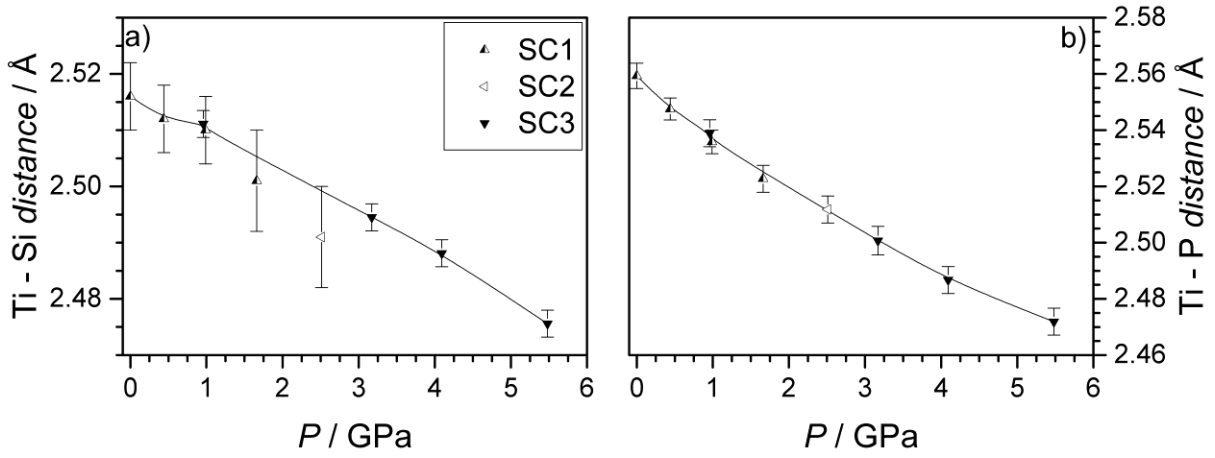

Figure 6. X-ray single-crystal diffraction studies of **8c** at variable pressure (0 – 5.5(1) GPa). The Ti-Si and Ti-P bonds show a different compressibility behavior at increasing pressures signaling their different chemical nature. The open and closed triangles symbolize three different single crystals (SC1-3) which were employed in three independent high pressure studies.

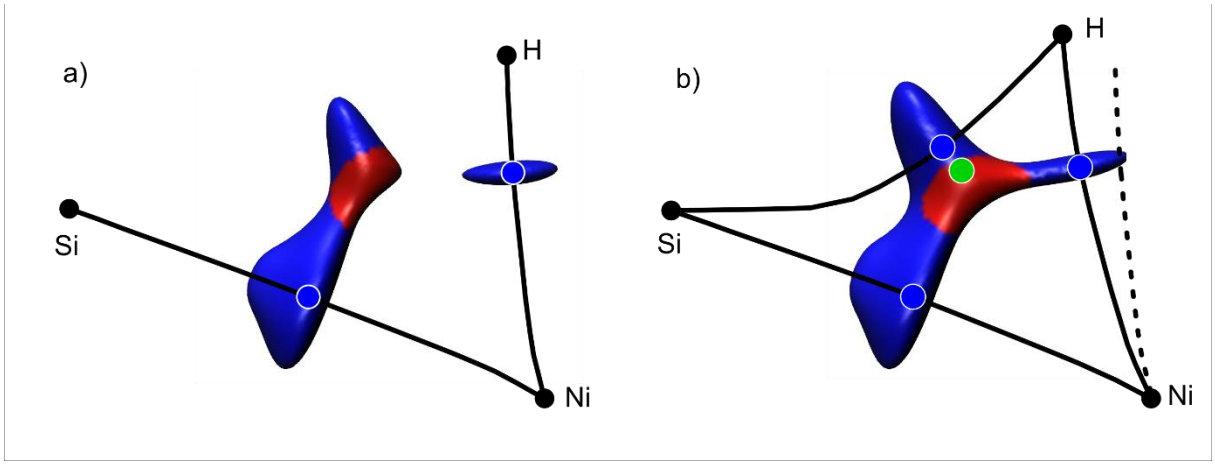

Figure 7. NCI isosurface plots (s(**r**)=0.2) for the Ni,Si,H moieties in compounds **6** (a) and **6'** (b) in a blue-red color scale of -0.05 au < sign(λ_2)ρ(**r**) < 0.05 au. Blue NCI domains are considered to mark regions where covalent interactions (λ_2<0) prevail while red contours signal domains where (λ_2>0). Bond paths are shown as black solid lines, BCPs as blue circles, RCPs as green circles and atoms as black circles. For better comparability, the Ni-H bond path of (a) is shown in (b) as a dashed line.

In Figure 7a the experimental sgn(λ_2)ρ(**r**) values are mapped onto the isosurfaces of the reduced density gradient s(**r**) of the Si-Ni-H moiety in **6**. Blue NCI domains are usually considered to mark regions where covalent interactions (λ_2<0) are dominant. For example, 2c2e covalent bonding domains are clearly revealed around the position of the Ni-Si and Ni-H BCP but also along the Si···H vector despite the lack of a Si-H_{br} BCP (Figure 5g). This clearly suggests the presence of residual covalent Si···H interactions. Indeed, the formation of the Si-H_{br} BCP can be enforced in a hypothetical model **6'** where the Si-H bond distance has been artificially shortened by 0.16 Å upon shifting the hydrogen atom parallel to the Ni-Si vector. In this model the blue NCI domains are located around the Si-H_{br} BCP and still closely resemble the shape and position of the domains in **6**, while the red domains are centered around the RCP. Hence, the nature of the Si···H_{br} interaction should be considered in terms of a "transition from bonding to non-bonding situations [which] is gradual instead of catastrophic".[14b] We note that red contours mark regions where (λ_2>0). It is usually considered that these red areas highlight regions where repulsive interactions prevail.[14] However, in case of ring systems the negative sign of λ_2>0 is a mathematical consequence of the presence of a ring critical point in the center of n-membered ring systems and should not necessarily interpreted as a signal of any repulsive interactions. As a matter of fact, the Si-H bond path in **6'** is inwardly curved. This scenario is clearly not signaling any repulsive interaction between the blue-marked regions around the Si-H BCP and the red-marked domains around the RCP.

A similar scenario is observed for Mn-Si interaction in the manganese complex **2** in line with theoretical predictions for the model systems $(CH_3)CpMn(CO)_2H(SiH_{3-n}Cl_n)$[14c] ($n$ = 0–3): the Mn-Si

BCP is present in the experimental charge density analyses but it disappears by an artificial stretching of the Mn-Si separation by 0.005 Å (See the Supporting information). Apparently, in the charge density picture complexes **1-7** represent a continuum of electronic structures along a single reaction coordinate.[5]

While the minute differences in the electronic structures of **1-7** could be safely revealed in the solid state by high resolution electron density studies it is tempting to search for an alternative methodology which is capable to provide similar tools also for compounds in solution. We will therefore present in the following experimental and theoretical NMR studies which complement these charge density studies and provide a tool box to analyze Si-H bond activation phenomena also in solution.

Experimental and Theoretical NMR Studies. Since the pioneering NMR studies by Corriou and Colomer in 1982,[16] the magnitude of $J(^{29}Si,^{1}H)$ spin-spin coupling constants has been employed to analyze the complex bonding scenarios displayed by transition metal hydrosilane complexes (Figure 1). The one-bond $^{1}J(Si,H)$ couplings in free hydrosilanes Si_nH_{2n+2} usually range from -192 to -203 Hz.[17] It is generally assumed that the Fermi-contact mechanism[18] provides the major contribution to the magnitude of these $^{1}J(Si,H)$ couplings while their negative sign is a natural consequence of the gyromagnetic ratio of the ^{29}Si nucleus (γ = -53.2×10^6 rads^{-1}T^{-1}).[17] Upon coordination to a transition metal the $|^{1}J(Si,H)|$ couplings decrease significantly compared with the corresponding free silane. This is illustrated in Figure 1 where the σ-silane complex $Cr(CO)_5SiH_2Ph_2$ **1** is characterized by a $^{1}J(Si,H)_{calc}$ value of -109 Hz while the corresponding value of the free ligand is significantly larger (-196 Hz). Accordingly, the magnitude of the $^{1}J(Si,H)$ couplings might provide a highly sensitive measure of Si-H bond activation processes even in the case of **1** which represents a σ-silane complex at the very early stage of the oxidative addition process. In addition, **1** is characterized by only a minute Si-H bond elongation of 0.08 Å relative to the free SiH_2Ph_2 ligand. In case of a complex representing the terminus of the oxidative addition process the Si-H bond is completely broken and the resulting $J(Si,H)$ couplings can be classified in terms of two-bond $^{2}J(Si,H)$ couplings. This scenario is evident in silyl hydride species such as $Fe(CO)_4H(SiCl_3)$[2b] **7** displaying a large Si-H separation of 2.64 Å and a positive $^{2}J(Si,H)$ coupling constant of +34 Hz. The positive sign of this $^{2}J(Si,H)$ coupling constant is in line with the negative gyromagnetic ratio of the ^{29}Si nucleus.[17]

The interpretation of $J(Si,H)$ couplings in nonclassical silane complexes (e.g. **3-6** in Figure 1) is however more complex. Already in 1990 Schubert proposed in a pioneering NMR study[3a] that bridging η^2(H-Si)*M* entities in these nonclassical silane complexes should be identified not only by geometrical criteria (e.g. short Si-H bond distances of less than 2.2 Å). The presence of noticeable covalent Si-H interactions in these systems should be also signaled by $|J(Si,H)|$ couplings significantly larger than 20 Hz. Unfortunately, the transition between classical and nonclassical hydrosilane complexes is a rather continuous one as outlined in the previous Section and the characteristic interval of $|J(Si,H)|$ coupling constants [20-70 Hz] originally proposed by Schubert[3a] to identify nonclassical silane complexes remains a matter of interpretation.[3g] Indeed, also our benchmark system **7** representing a classical silyl hydride yields a positive $J(Si,H)$ coupling which violates the rather arbitrary 20 Hz limit in theory (+34 Hz) and experiment (22 Hz; Figure 1).[19] The situation is further complicated by the presence of bridging η^2(H-Si)*M* entities. In that case Corriou and Colomer proposed that the total coupling constant formally emerges from a competing one- and two bond coupling mechanism: $J(Si,H) = {}^{1}J(Si,H) + {}^{2}J(Si,M,H)$.[16] Since the signs of one bond and two bond ^{29}Si-^{1}H couplings should be opposite ($^{1}J(Si,H) < 0$ and $^{2}J(Si,M,H) > 0$) the observed $J(Si,H)$ coupling constants might even vanish if both coupling components are of equal magnitude. Hence, the magnitude of the $J(Si,H)$ couplings alone cannot be taken as a measure of the σ(Si-H) interaction strength and its degree of covalency. Accordingly, Ignatov et al. proposed that only a negative $J(Si,H)$ sign provides "conclusive evidence of the presence of a direct Si-H bond"[10a] by signaling the predominance of the $^{1}J(Si,H)$ contribution. However, we point out already at this stage that the discrimination of one-bond and two-bond couplings in three-membered rings is not possible in the framework of the Fermi-contact mechanism.[5] In the next step we will therefore solely interpret the signs and magnitudes of the total $J(Si,H)$ couplings and avoid the confusing discussion of any one- or two-bond coupling mechanisms.

As outlined above one might expect a change of sign of the $J(Si,H)$ couplings in hydrosilane complexes from negative to positive along the reaction coordinate of the oxidative addition. Indeed, inspection of Figure 1 reveals such a $J(Si,H)$ sign crossover between the titanium d^2 complex $Cp_2Ti(PMe_3)HSiHPh_2$ **4** and the electronically closely related species $Cp_2Ti(PMe_3)HSiHPhCl$ **5**.[5] The respective $J(Si,H_{br})$ values change from -28Hz to +23 Hz in the order **4→5**. In line with the charge density analysis (see above), the introduction of one electronegative chloro substituent at the silicon atom enhances the degree of oxidative addition of the Si-H bond to the metal atom. A similar trend is observed for the $J(Si,H_{br})$ couplings in case of the complexes **2→3** (Figure 1). The according $J(Si,H_{br})$ values increase from -68 Hz to -52Hz in the order **2→3** and reflect again the promotion of the oxidative addition of the Si-H bond to the metal atom by electron-withdrawing substituents at the silicon atom. However, the $J(Si,H_{br})$ coupling remains negative in **3** in contrast to complex **5** since the degree of covalency of the Si-H bond is significantly larger in case of the manganese complex. Hence, the grouping of ASOAP complexes **2→3→4→5** along the reaction coordinate of

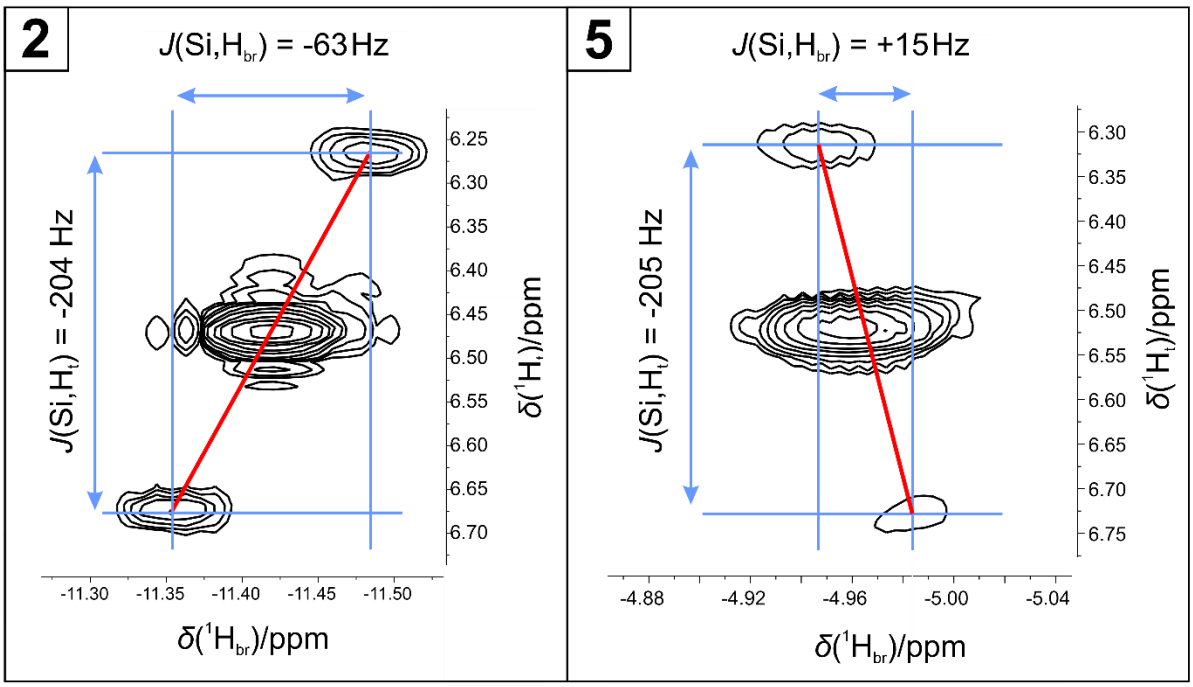

Figure 8. a) Salient details of the cross-peaks in the 500 MHz ^{1}H-^{1}H-COSY spectrum of the manganese d^{6}-complex **2** and the titanium d^{2} complex **5**. The red solid lines interconnect the centers of the two ^{29}Si-satellites next to the ^{1}H signal of the bridging *M*-H$_{br}$-Si moiety in both compounds. From its positive/negative slope one can conclude that the individual ^{1}J(Si,H$_t$) and J(Si,H$_{br}$) coupling constants are of same/opposite sign in **2** and **5**, respectively (ref 20). Since ^{1}J(Si,H$_t$) < 0 (ref 17) the sign of J(Si,H$_{br}$) must be negative (-63 Hz) in **2** and positive (+15 Hz) in **3**.

the oxidative addition in Figure 1 is in line with both charge density analysis and the interpretation of the signs of the respective J(Si,H$_{br}$) couplings.

In the next step of our analysis we have tried to support these NMR trends based on theoretical data by experimental determinations of the J(Si,H) signs in **2** and **5** (Figure 8). **2** and **5** are suitable model systems since both display a non-coordinating *terminal* Si-H$_t$ moiety characterized by a negative ^{1}J(Si,H) coupling constant which can be used as internal reference for an unequivocal sign determination of J(Si,H$_{br}$) of the *bridging* Si-H$_{br}$ group. Indeed, analysis of the individual J coupling contributions to the cross-peak multiplet of the three-spin system (^{1}H$_t$, ^{1}H$_{br}$, ^{29}Si) (Figure 8) finally allowed the J(Si,H)$_{exp}$ sign determination of -63 Hz and +15 Hz in case of **2** and **5**, respectively, in agreement with the DFT predictions (-68Hz and +23Hz, respectively).

Since the experimental NMR studies support the theoretical findings we also tried to connect these trends with the topology of the electron density distributions as introduced in the previous Section. Inspection of the electron density maps in the molecular (*M*,Si,H$_{br}$) plane reveals a clear trend: The *M*-Si BCP is absent in the manganese σ-complex **2** and is just forming in the manganese complex **3**. In line with the NMR results **3** occurs at a later stage of the oxidative addition reaction coordinate than **2** due to the promoted $M\rightarrow\sigma^{*}$(H-Si-*X*) back donation in **3** (*X* = F in **3** and H in **2**). However, as outlined above the *M*-Si bond path in **3** is still close to a catastrophe scenario (Figure 5a,b). The degree of the $M\rightarrow\sigma^{*}$(H-Si-*X*) back donation is however further increased in the early transition metal d^{2} complexes **4** and **5** as witnessed by a larger separation of the *M*-Si BCP and the corresponding RCP (Figure 5c,d and the Supporting Information). This again is reflected by the shift of the J(Si,H$_{br}$) couplings from negative to positive values. In the Ni-complex Ni(*i*Pr$_2$Im)$_2$(H)(SiMePh$_2$) (**6** in Figure 1) both, the Ni-Si and Ni-H bond formation process is almost complete. As a consequence the Si-H bond is nearly broken as signaled by the large Si-H bond distance of 2.09 Å and a positive J(Si,H) value of +47 Hz.[3i,4d] Accordingly, we propose that the position of hydrosilanes along the reaction coordinate of the oxidative addition can be identified either by topological analysis of the electron density or complementary via interpretation of sign and magnitude of the J(Si,H) coupling constants.

To find further support for this hypothesis we continued to analyze the NMR properties of the substitution series Cp$_2$Ti(PMe$_3$)(HSiMe$_{3-n}$Cl$_n$) **8a-d** and (CH$_3$)CpMn(CO)$_2$(HSiMe$_{3-n}$Cl$_n$) **9a-d** and the respective free hydrosilanes (HSiMe$_{3-n}$Cl$_n$) (n = 0-3) (Figure 9; Scheme 1).

We first note that the model systems **8a**/**8b** and **9a**/**9b** display similar trends with regard to their J(Si,H) couplings in comparison with our experimental benchmark systems **2**, **3**, **4** and **5**. Indeed, introduction of an electronegative group at the silicon atom shifts the J(Si,H) couplings to more positive values: **9a** (-66 Hz) → **9b** (-36 Hz) and **8a** (-24 Hz) → **8b** (+21 Hz). In contrast, the free silane ligands show the reverse trend and display a monotonic decrease of the J(Si,H) couplings from -183 Hz in HSiMe$_3$ to -367 Hz in HSiCl$_3$. The electronic origin of these trends displayed by the free silanes was

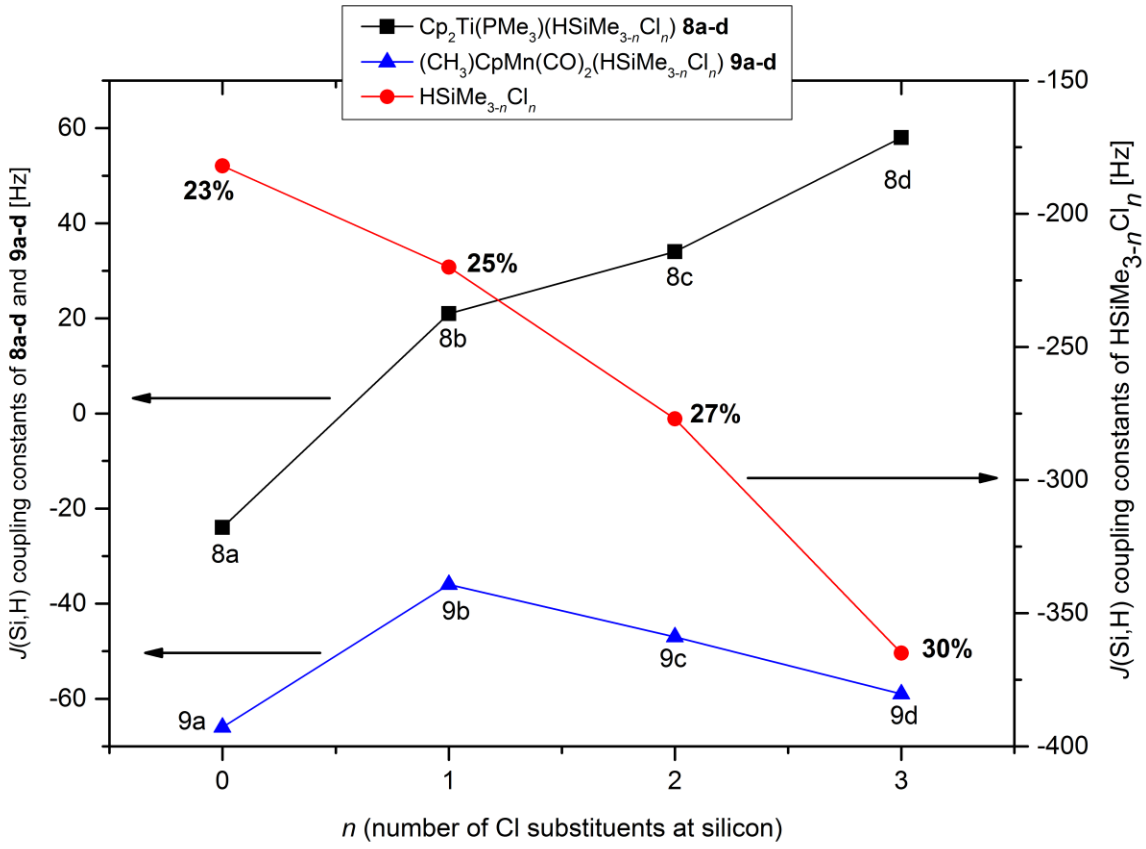

Figure 9. Influence of electronegative chlorine substituents at the silicon atom on the *J*(Si,H) couplings in the free silanes $SiMe_{3-n}Cl_n$ and the respective metal complexes $Cp_2Ti(PMe_3)(HSiMe_{3-n}Cl_n)$ **8a-d**; $(CH_3)CpMn(CO)_2(HSiMe_{3-n}Cl_n)$ **9a-d** (n = 0-3). In case of the free hydrosilanes the percentage of *s* character in the sp^x silicon hybrids forming the respective Si-H bond is specified in bold numbers and was obtained by NBO analyses (ref 21).

discovered already in the year 1959 by Muller and Pritchard in ^{1}H NMR studies of the related $HCH_{3-n}Cl_n$ (n = 0-3) substitution series.[22a] The authors concluded that the $|^1J(C,H)|$ values are approximately proportional to the degree of *s* character in the carbon hybrid orbital bonded to the hydrogen atom - provided the Fermi contact mechanism is the dominant one. This concept was later used to formulate Bent's rule[23] and finally extended by Ebsworth to explain substitution effects on $|^1J(Si,H)|$ couplings in the free silanes $HSiH_{3-n}X_n$ (n = 0-3; X = F, Cl, Br, I).[24] Indeed, a natural bond orbital analysis[21] (Figure 9) reveals a high correlation between the percentage of *s* character of the σ(Si-H) NBO and the $|^1J(Si,H)|$ coupling constants in case of the free silanes $HSiMe_{3-n}Cl_n$ (n = 0-3). This can be explained by the fact that (*i*) the Fermi contact contribution is proportional to the product of the core (cusp) electron densities of the two bonding atomic orbitals or hybrids of the silicon and hydrogen atoms. Since only *s*-orbitals contribute to the cusp at Si and H this contact contribution is (*ii*) directly proportional to the percentage of *s* character in the sp^x silicon hybrids forming the respective Si-H bonds in $HSiH_{3-n}Cl_n$ (n = 0-3). In line with Bent's rule the increasing $|^1J(Si,H)|$ values in the series $HSiH_{3-n}Cl_n$ are therefore linked with the increasing number n of electronegative chlorine substituents[17] which increase the s/p ratio in the sp^x silicon hybrid in the corresponding σ(Si-H) NBOs of the free hydrosilanes ($HSiMe_{3-n}Cl_n$) (n = 0-3).[25]

However, this simple and successful concept of Muller and Pritchard loses its predictive power when hydrosilanes enter the coordination sphere of organometallic fragments (Figure 9). Apparently a more sophisticated methodology is needed to identify the electronic control parameters of *J*(Si,H) couplings in hydrosilane metal complexes. Especially, the shift of the *J*(Si,H) couplings to more positive values from **8a** → **8b** and **9a** → **9b** warrants clarification. We therefore analyzed the individual molecular orbital (MO) contribution to the isotropic coupling caused by the Fermi-contact mechanism using a density functional method developed by Autschbach and Ziegler.[26] For the analytic calculation of nuclear spin-spin coupling constants the relativistic zero-order regular approximation (ZORA) was employed.[27] With the Autschbach/Ziegler approach (Formula 2)[26] it is possible to decompose the *J*(Si,H) couplings into individual contributions from pairs of occupied and virtual MOs.

$$J_{\sigma/\pi}(Si,H) \sim (-1) \times const. \times \frac{c_0(Si)c_v(Si) \times c_0(H)c_v(H)}{\varepsilon_0 - \varepsilon_v} \quad (2)$$

In Equation 2 the negative prefactor (-1) considers the negative gyromagnetic ratio of the silicon atom while $c_0(X)$ and $c_v(X)$ (X = Si or H) are the coefficients of the atomic orbitals of the silicon and hydrogen atom in the

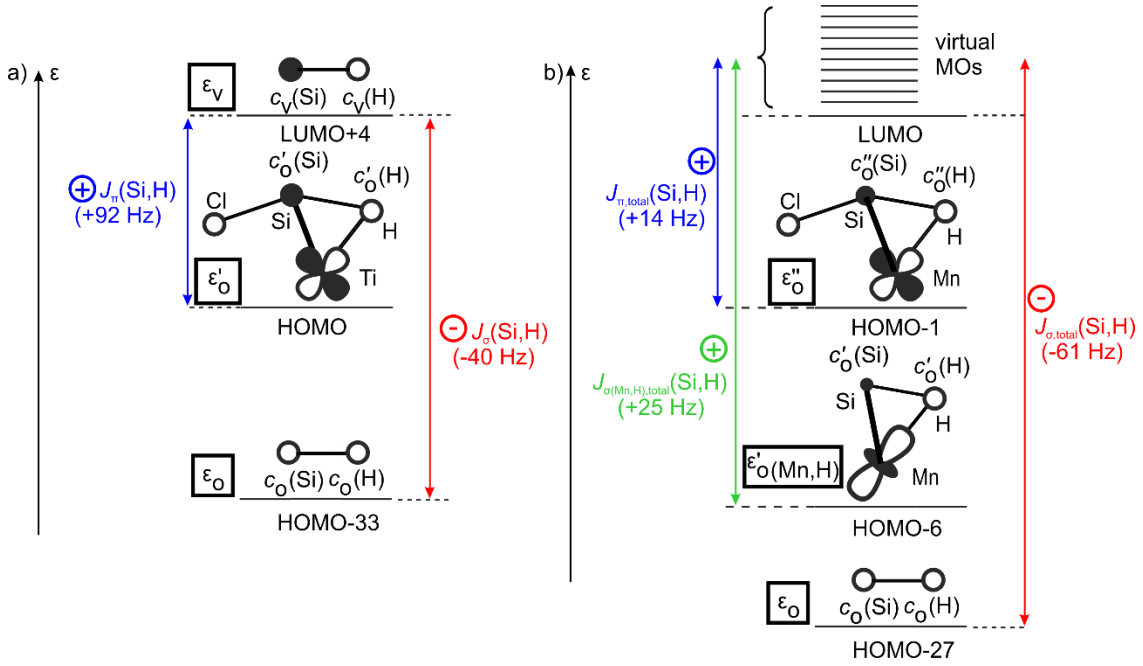

Figure 10. a) Decomposition of the J(Si,H) couplings of $Cp_2Ti(PMe_3)(HSiCl_3)$ (**8d**) into individual J_σ(Si,H) and J_π(Si,H) contributions from pairs of interacting occupied and virtual MOs. The notation J_σ(Si,H) denotes the mixing between the bonding σ(Si-H) and vacant σ^*(Si-H) orbital which yields a negative contribution to the global J(Si,H) coupling of **8d**. The mixing of the occupied HOMO (which is responsible for the $M\rightarrow L$ π back donation) and the vacant σ^*(Si-H) orbital (LUMO+4) is labeled J_π(Si,H) and provides a positive and dominant contribution to the Fermi contact term of J(Si,H) in **8d**. Note that only predominant orbital interactions of the Fermi contact terms are considered in this schematic drawing; b) Decomposition of the J(Si,H) couplings of $(CH_3)CpMn(CO)_2(HSiMe_2Cl)$ (**9b**) into individual $J_{\sigma,total}$(Si,H) and $J_{\pi,total}$(Si,H) contributions from pairs of interacting occupied and virtual MOs. The index "total" specifies that *all* interactions between *all* virtual orbitals and the respective occupied orbitals (HOMO-27, HOMO-6 and HOMO-1) are considered. The mixing of the occupied σ(Si-H) orbital (HOMO-27) with all vacant orbitals provides the dominating coupling contributions $J_{\sigma,total}$(Si,H) to the (negative) Fermi contact term J(Si,H) in **9b** (Table 1).

respective occupied and virtual orbitals which are separated by the energy gap $\varepsilon_o - \varepsilon_v$. $J_{\sigma/\pi}$(Si,H) denotes individual coupling contributions from pairs of interacting orbitals where the indices σ/π specify the nature of the respective occupied orbitals. Accordingly, the notation J_σ(Si,H) was used in Figure 10a to denote the mixing between the bonding σ(Si-H) and vacant σ^*(Si-H) orbital while the term J_π(Si,H) depends on the mixing of the occupied HOMO (which is responsible for the $M\rightarrow L$ π back donation) and the vacant σ^*(Si-H) orbital (LUMO+4). Since the prefactor and energy difference term $(\varepsilon_o - \varepsilon_v)$ in Equation 2 are both negative , the sign of the resulting $J_{\sigma/\pi}$(Si,H) coupling constants depends solely on the sign of the orbital overlap term – provided the Fermi contact mechanism is the dominant one.

We start our analysis with the titanium model system **8a** (Figure 10a). According to Equation **2** the positive sign of the J_π(Si,H) contribution (+92 Hz) is due to the nodal plane in the Ti→σ^*(H-Si-Cl) π back bonding orbital (HOMO; Figure 10a) which causes the overlap term $[c_o(Si)c_v(Si) \times c_o(H)c_v(H)]$ and therefore also the sign of J_π(Si,H) to become positive. In contrast, the corresponding J_σ(Si,H) contribution which emerges from the interaction between the occupied and low-lying σ(Si-H) bonding orbital with the virtual LUMO+4 orbital (-40 Hz) is negative and small compared to J_π(Si,H). The larger | J_π(Si,H) | vs | J_σ(Si,H) | value can be also explained by Equation **2** and is a consequence of the energy penalty (ε_σ-ε_{σ^*}) which is larger for the J_σ(Si,H) vs J_π(Si,H) coupling contributions due to the large energy separation between σ(Si-H) and σ^*(Si-H). The sum of both components J_π(Si,H) (+92 Hz) and J_σ(Si,H) (-40 Hz) finally yields the coupling constant J(Si,H) of +52 Hz which approaches the total J(Si,H) coupling constant of +58 Hz (which considers all orbital interactions) closely (Table 1). Hence, the interactions of the chemically most relevant bonding orbitals, namely Ti→σ^*(H-Si-Cl) and σ(Si-H), with just one of the virtual orbitals (LUMO+4) of **8d** helps us to understand the complex origin of the J(Si,H) sign in this nonclassical silane complex. This implies that the sign of J(Si,H) couplings in transition metal silane complexes might simply reflect the electronic competition between (negative) J_σ(Si,H) and (positive) J_π(Si,H) orbital interactions.

In order to get a more comprehensive picture also for the remaining members of the series $Cp_2Ti(PMe_3)(HSiMe_{3-n}Cl_n)$ (n = 0-3) **8a-d** we analyzed all coupling contributions from the interactions between their occupied σ(Si-H) and Ti→σ^*(H-Si-Cl) orbitals with the complete set of virtual orbitals.[5] These contributions are denoted $J_{\sigma,total}$(Si,H) in the following. We learn from Table 1 that these negative $J_{\sigma,total}$(Si,H) couplings do not vary significantly with the number of chloro substituents -67 Hz (**8a**, n=0); -64 Hz (**8b**, n=1); -64 Hz (**8c**, n=2) and -65 Hz (**8d**, n=3). This observation might be

Table 1. Contributions to the Fermi contact term *J*(Si,H) from the mixing of occupied and vacant orbitals in 8a-d and 9a-d

Coupling contributions (Hz)	**8a**	**8b**	**8c**	**8d**	**9a**	**9b**	**9c**	**9d**
$J_{\sigma,total}$(Si,H)	-67	-64	-64	-65[a]	-82	-61	-72	-80
$J_{\sigma(Mn,H),total}$(Si,H)	-	-	-	-	+23	+25	+18	+3
$J_{\pi,total}$(Si,H)	+51	+73	+99	+144[a]	+6	+14	+20	+41
other MO interactions	-8	+12	-1	-21	-13	-14	-13	-23
total J(Si,H) [b]	-24	+21	+34	+58	-66	-36	-47	-59

[a] Only the interaction with the virtual σ^*(Si-H) MO has been considered in Figure 10a; [b] only coupling contributions from the Fermi contact (FC) spin-spin coupling mechanism are considered. The *total J*(Si,H) values change only marginally (by less than ± 2Hz) when also the spin-dipole (SD), paramagnetic orbital (OP), and diamagnetic orbital (OD) terms are included.

connected with the fact that also the Si-H bond distances of these models are hardly influenced by the number of chloro substituents *n* (Figure 4): 1.825 Å in **8a** (*n*=0); 1.820 Å in **8b** (*n*=1); 1.822 Å in **8c** (*n*=2) and 1.848 Å in **8d** (*n*=3).[28] Hence, the negative $J_{\sigma,total}$(Si,H) couplings in **8a-d** signal the presence of significant covalent Si-H interactions in the Ti,Si,H metallacycles in line with the classification of **8a-8d** as ASOAPs. We note that the slight decrease of these values from **8b-8d** with increasing number of chloro ligands is in line with Bent's rule and follows the trends observed for *J*(Si,H) values of the respective free hydrosilanes $HSiMe_{3-n}Cl_n$ (Figure 9). However, this effect is small and overcompensated by the sharp increase of the J_π(Si,H)-type coupling contributions with increasing substitution degree *n*: +51 Hz in **8a** (*n*=0); +73 Hz in **8b** (*n*=1); +99 Hz in **8c**, (*n*=2) and +144 Hz in **8d** (*n*=3).

Accordingly, the increasing *J*(Si,H) values and the sign change from negative (**8a**) to positive (**8b-d**) is mainly due to the enhancement of the positive J_π(Si,H) contribution with increasing number of chlorine substituents at the silicon atom. This again reflects the increasing dominance of the Ti→σ^*(H-Si-Cl) π-back donation in the series **8a-d** in line with our conclusions based on charge density analyses (see above). We note that the observed trends in *J*(Si,H) values do not depend on the presence or absence of interligand-hypervalent interactions (IHI).[3e,10a] Such interactions would rely on a pronounced σ(Ti-H)→ σ^*(Si-Cl) orbital interaction mechanism which could not be identified.[5,29] We further note that a related trend has been also found in case of the substitution series $Cp(ArN)Ta(PMe_3)(H)(SiMe_{3-n}Cl_n)$ **10a-10d**[10b] (*n* = 0-3) (Scheme 1). The corresponding theoretical *J*(Si,H) values are +24 Hz (**10a**), +36 Hz (**10b**), +46 Hz (**10c**) +58 Hz (**10d**).[30] However, the degree of oxidative addition in the d^2 tantalum complexes is significantly larger compared with the titanium species **8a-8d**. The Si-H bonds in **10a-10d** (*r*(Si-H) = 2.207-2.239Å) are therefore significantly longer compared with the ones in **8a-8d** (1.820-1.848Å). As a consequence, all complexes of this series (inclusive **10a**) display positive *J*(Si,H) values in line with the predominance of the J_π(Si,H)-type coupling contribution.

The final step of our coupling analysis aims at the origin of the decreasing *J*(Si,H) values in the d^6 manganese complexes $(CH_3)CpMn(CO)_2(HSiMe_{3-n}Cl_n)$ (*n* =1-3; **9b-d**) (Figure 9) with increasing *n*. Table 1 shows that in case of the electron-rich d^6 complexes also orbital interactions between the bonding σ(Mn-H) and virtual orbitals need to be considered. This positive coupling contribution is denoted $J_{\sigma(Mn,H),total}$(Si,H) in Figure 10b and the decreasing *J*(Si,H) values of **9b-d** can be explained by inspecting the individual $J_{\sigma,total}$(Si,H), $J_{\sigma(Mn,H),total}$(Si,H) and $J_{\pi,total}$(Si,H)-type contributions. In contrast to **8a-d**, the negative J_σ(Si,H)-type contributions are predominant in **9a-d**. This underpins – in line with the charge density analysis – the larger degree of covalent Si-H bond character in the d^6-manganese complexes **9a-d** relative to **8a-d**. Similar to **8a-8d** we also find in **9a-d** a systematic increase of the positive $J_{\pi,total}$(Si,H)-type contributions with growing number of chlorine substituents (*n*) at the silicon atoms. This interaction is again mainly responsible for the increase of the absolute *J*(Si,H) values from **9a** (-66 Hz) to **9b** (-36 Hz). However, along the series **9b** (-36 Hz)→**9c** (-47 Hz)→**9d** (-59 Hz) the absolute *J*(Si,H) couplings decrease. Apparently, the increasing positive coupling contribution of $J_{\pi,total}$(Si,H) is partially compensated by the decreasing positive $J_{\sigma(Mn,H),total}$(Si,H) contributions. As a consequence the sum of both types of positive coupling contributions remains rather constant in **9b-d** and the *J*(Si,H) couplings are virtually dependent on the $J_{\sigma,total}$(Si,H) contributions alone. These values decrease (as outlined above in case of **8b-d**) with the increasing chloro substitution degree *n* from -61 Hz to -80 Hz in line with Bent's rule. Due to the pronounced covalent character of the Si-H bonds in the d^6 manganese complexes this trend predominates the total *J*(Si-H) couplings. As a consequence, the series **9b→9c→9d** shows a similar dependency of the *J*(Si-H) couplings on the chloro substitution degree *n* as the corresponding free silane ligands (Figure 9).

CONCLUSION

Detailed charge density studies reveal that transition metal hydrosilane complexes display a continuum of electronic structures. This can be explained in terms of an extended Dewar-Chatt-Duncanson (DCD) model where σ-hydrosilane complexes are characterized by their predominant $M\leftarrow\sigma(Si\text{-}H_{br})$ donation while the propagation along the oxidative addition pathway in non-classical silanes is triggered by the increasing extent

of the $M \rightarrow \sigma^*(H_{br}\text{-Si-}X)$ back donation (X = electron withdrawing substituent at the silicon atom; H_{br} = bridging hydrogen atom). The reaction coordinate of this oxidative addition process can be determined by electron density studies in the solid state or alternatively by the sign and magnitude of *J(Si,H)* couplings in solution NMR studies. In the latter case a simple structure-property relationship emerges: a positive sign of $J(Si,H_{br})$ coupling constants is due to the predominance of the $J_\pi(Si,H_{br})$ coupling contributions and signal the presence of pronounced $M \rightarrow \sigma^*(H_{br}\text{-Si-}X)$ π-back donation in the respective silane complexes. These complexes can be characterized as silane species close to the final stage of the oxidative addition trajectory. In contrast *negative* $J(Si,H)$ values signal the dominance of $J_\sigma(Si,H)$ coupling contributions and hint for the presence of significant covalent Si-H interactions. The respective silane complexes therefore reside at an earlier stage of the oxidative addition reaction trajectory. Hence, in non-classical hydrosilane complexes such as $Cp_2Ti(PMe_3)(HSiMe_{3-n}Cl_n)$ (with n=1-3) the sign of $J(Si,H)$ changes from *minus* to *plus* with increasing number of chloro substituents n and maps the gently rising extent of oxidative addition. On contrary, in the series $(CH_3)CpMn(CO)_2(HSiMe_{3-n}Cl_n)$ the $J(Si,H)$ remain negative due to the large extent of covalency of the Si-H_{br} bond. Here, the decrease of the absolute $J(Si,H)$ values with increasing chloro substitution degree n from -61 Hz to -80 Hz is in line with Bent's rule – as secondary control parameter of the $J(Si,H)$ couplings. We finally note that in all case studies the $J(Si,H_{br})$ couplings are not significantly affected by the presence/absence of additional interligand hypervalent interactions.

EXPERIMENTAL AND COMPUTATIONAL SECTION

General methods and materials. All manipulations of air-sensitive compounds were performed in an atmosphere of dry argon either on a dual-manifold Schlenk line, interfaced with a high-vacuum (10^{-3} Torr) line, or in a MBraun glove box. Solvents (n-hexane, THF, toluene) were dried and degassed by using a MBraun solvent purification system. Dichloromethane was distilled from P_2O_5 and stored over Linde type 4A molecular sieves. Deuterated solvents were purchased from Deutero GmbH (>99.5 atom % D). All solvents were stored under argon. Standard 1D NMR experiments were performed at a MERCURYplus 400 High Resolution System from VARIAN Deutschland GmbH. The determination of the signs of the coupling constants via 2D NMR methods was performed employing a Bruker Avance II+ 500 spectrometer at the University of Tübingen. Chemical shifts are referenced to the residual solvent peaks and are reported in ppm relative to tetramethylsilane. IR spectra were recorded on a Thermo Nexus FT-IR spectrometer modified with a Specac Heated Golden Gate™ MKII ATR setup (GS10542). Elemental analyses were carried out with an ELEMENTAR vario EL III. All hydrosilanes, Cp_2TiCl_2, PMe_3, 1,2-Dibromoethane and magnesium turnings were purchased from Sigma-Aldrich, $[Ph_3C]BF_4$ from Alfa Aesar. $Cp_2Ti(PMe_3)_2$ was prepared by the method of Kool et al.[31] The manganese complexes $(CH_3)CpMn(CO)_2(HSiHPh_2)$ (**2**), $(CH_3)CpMn(CO)_2(HSiFPh_2)$ (**3**) were synthesized according to slightly modified literature procedures.[4a]

Synthesis of $(CH_3)CpMn(CO)_2(H_2SiPh_2)$ (2). A solution of $(CH_3)CpMn(CO)3$ (436 mg, 2 mmol) and H_2SiPh_2 (368 mg, 2 mmol) in hexane (25 mL) was irradiated with UV light for 1 h. The flask was equipped with a pressure relief valve to allow the emerging CO to leave the reaction vessel. After the reaction was complete the solution was filtered and the yellow filtrate was reduced in vacuo to 5 mL. At -78 °C the product precipitated as a light yellow solid, which was isolated and washed with small portions of hexane. Yield = 112 mg, 0.3 mmol, 15 %; ^{1}H NMR (400 MHz, $CDCl_3$, 20 °C): δ = 7.64 – 7.31 (m, 10 H; C_6H_5), 6.25 (d, ^3J (HMnSiH) = 4.8 Hz, 1 H; SiH_t), 4.40 (d, 4 H; C_5H_4), 2.0 (s, 3 H; CH_3), -11.5 (d, ^3J (HMnSiH) = 4.8 Hz, 1 H; MnH_{br}Si). ^{13}C{^{1}H} NMR (101 MHz, $CDCl_3$, 20 °C): δ = 227.6 (*C*O), 140.6 - 127.8 (C_6H_5), 101.9 - 83.3 (C_5H_4), 13.3 (CH_3). ^{29}Si NMR (79 MHz, $CDCl_3$, 20°C): δ = 13.1 (d+d, ^1J (Si,H_t) = |207| Hz, ^2J (H_{br}MnSi) = |63| Hz). IR: $\tilde{\nu}$ = 1905, 1967 cm^{-1} (C=O). Elemental analysis calcd (%) for $C_{20}H_{19}MnO_2Si$: C 64.16, H 5.11; found: C 62.06, H 4.82.

Synthesis of $(CH_3)CpMn(CO)_2(HSiFPh_2)$ (3). A solution of **2** (0.56 g, 1.5 mmol) and $[Ph_3C]BF_4$ (0.5 g, 1.5 mmol) in Dichloromethane (25mL) was stirred at RT for 1 h. The solution was filtered and the solvent was removed in vacuo. The residue was dissolved in 2 ml of hexane, filtered and stored at -30°C. After 16 h the product was obtained as light yellow crystals, which were isolated and washed with small portions of hexane. ^{1}H NMR (400 MHz, [D_8]toluene, 20 °C): δ = 7.76 – 7.15 (m, 10 H; C_6H_5), 3.97 (m, 4 H; C_5H_4), 1.50 (s, 3 H; CH_3), -12.03 (d, ^3J (HMnSiF) = 6.3 Hz, 1 H; Si*H*). ^{29}Si NMR (79 MHz, [D_8]toluene, 20 °C): δ = 60.7 (d+d, ^2J (HMnSi) = |57| Hz, ^1J (Si, F) = |333| Hz). ^{19}F NMR (376 MHz, [D_8]toluene, 20 °C): δ = -127. IR: $\tilde{\nu}$ = 1897, 1990 cm-1 (C=O);

Synthesis of Cp2Ti(PMe3)(HSiHPhCl) (5): A solution of $H_2SiPhCl$ (0.1 mL, 0.2 mmol) in hexane (1.5 mL) was added to a solution of $Cp_2Ti(PMe_3)_2$ (60 mg, 0.2 mmol) in toluene (4.5 mL). After a few minutes yellow-orange crystals were formed, which were isolated and washed with small portions of hexane. ^{1}H NMR (400 MHz, [D_8]toluene, -30°C): δ = 8.19 – 6.99 (m, 5 H; C_6H_5, overlayed with solvent signals), 6.49 (d, ^3J (HTiSiH) = 6.0 Hz, 1 H; SiH_t), 4.89 (s, 5 H; C_5H_5), 4.63 (s, 5 H; C_5H_5), 0.50 (d, ^2J (P,H) = 6.2 Hz, 9 H; PMe_3), -4.93 (d+d, ^2J (P,H) = 73.4 Hz, J (HTiSiH) = 6.0 Hz, 1 H; TiH_{br}Si). ^{31}P{^{1}H} NMR (202 MHz, [D_8]toluene, -30°C): δ = 19.19 (s+d, ^2J (Si,P) = 31 Hz). ^{29}Si NMR (79 MHz, [D_8]toluene, -30°C): δ = 75.7 (d, ^1J (Si,H_t) = 205 Hz). Elemental analysis calcd (%) for $C_{19}H_{26}TiPSiCl$: C 57.51, H 6.60; found: C 56.50, H 6.37.

Computational Details. The geometries of all compounds have been optimized with ADF[32] at the PBE0 level[33] of theory in combination with an all-electron TZ2P basis set[34] and the ZORA Hamiltonian to describe

scalar relativistic effects[35]. A single point SCF-calculation was carried out on those geometries employing a larger basis set on the Si and the H atom for which J(Si,H) was calculated: for the H atom the jcpl basis set as implemented in ADF was used, while for Si the TZ2P basis set was augmented with additional basis functions analogue to the jcpl basis set for H. The calculation of the coupling constants was carried out in ADF.[26,36] The results discussed in the manuscript consider only the Fermi-contact mechanism, while the J(Si,H) coupling constants including the contributions of all Ramsey-terms[18] are presented in the Supporting Information. The analysis of the electron density in the framework of the QTAIM was carried out with ADF.[37] NBO analyses have been performed employing the ADFNBO module implemented in the ADF suite of programs.[21] The MO-plots in Figure 2 and 3 were calculated with Dgrid[38] and the 2D slices of $L(\mathbf{r}) = -\nabla^2\rho(\mathbf{r})$ in Figure 5b,d,f,h were determined with the Denprop-Code.[39]

X-RAY CRYSTALLOGRAPHY

X-ray data collection. A yellow, transparent block of $Cp_2Ti(PMe_3)(HSiMeCl_2)$ (**8c**) with dimensions 0.130 × 0.141 × 0.180 mm was coated with perfluorinated ether under an inert gas atmosphere and mounted on a BRUKER SMART-APEX diffractometer with D8 goniometer (Ag Kα radiation; λ = 0.56087 Å; Incoatec IμS 1.0) equipped with a low-temperature device. The sample was then cooled to 100(2) K by putting the crystal under the cold stream at target temperature. Intensity data were collected employing an APEX II CCD detector and 40 ω-scans over 180° with 0.5° (low order) and 0.25° (high order) slicing, a detector-to-sample distance of 50 mm and scan times between 3 seconds and 180 seconds.

X-ray data reduction. Crystal data for **8c** at 100(2) K: M_r = 369.18 g/mol, triclinic, space group P-1 (Int. Tables No. 2), a = 8.2102(12), b = 8.8057(13), c = 12.9105(19) Å, α = 83.348(5)°, β = 88.217(5)°, γ = 64.552(5)°, V = 837.0(2) Å^3, Z = 2, F(000) = 384, D_{calc} = 1.465 g cm^{-3}, μ = 0.50 mm^{-1}. Cell refinement and data integration were performed with SAINT[40], resulting in a total of 276398 measured reflections. An empirical ("multi-scan") absorption correction was applied [T_{min} = 0.8491, T_{max} = 0.8922] using SADABS.[41] The internal agreement factor was $R_{int}(F)$ = 0.044 yielding 22086 unique reflections. The full data set provided a completeness of 98.2% in the data range from 4.066° < 2θ < 82.058° ($\sin\theta_{max}/\lambda$ = 1.17 Å^{-1}).

Multipolar refinements and determination of the deformation density. First, an independent atom model (IAM) refinement was carried out using SHELXL[42]. Anisotropic thermal parameters were introduced to describe the thermal motion of all non-hydrogen atoms. The refinement finally converged at R_1 = 0.0261, wR_2 = 0.0661 and $GooF$ = 1.037 for all reflections and 180 parameters. A multipole model was then adopted to describe the aspherical charge density deformation of $\rho(\mathbf{r})$.

According to a method proposed by Stewart,[43] the electron density $\rho(\mathbf{r})$ in a crystal is described by a sum of aspherical pseudoatoms at the nuclear positions $\{\mathbf{R}_j\}$.

$$\rho(\mathbf{r}) = \sum_j \rho_j(\mathbf{r} - \mathbf{R}_j)$$

Based on the Hansen-Coppens formalism,[15] the pseudoatom density ρ_{at} is expressed in terms of multipoles:

$$\rho_{at}(\mathbf{r}) = P_c\rho_{core}(r) + P_v\kappa^3\rho_{valence}(\kappa r) + \sum_{l=0}^{l_{max}}\kappa'^3 R_l(\kappa' r)\sum_{m=0}^{l} P_{lm\pm}d_{lm\pm}(\theta,\phi)$$

In the refinement of our best model the multipole expansion was truncated at the hexadecapole level (l_{max} = 4) for all atoms except hydrogen. A bond-directed dipole and quadrupole (l_{max} = 2) was introduced for the hydrogen atoms. For the bridging hydrogen H(11) two bond-directed dipoles were used (l_{max} = 1). Core and spherical valence densities were constructed using relativistic wave functions, which are expanded over Slater-type basis functions, as implemented in the databank-file of Volkov and Macchi (VM) provided by the XD2006 suite of programs.[44] Single- ξ functions were also taken from the VM databank. The valence configuration of Ti was selected between two different models with [4s^{0}3d^4] and [4s^{2}3d^2] configuration. In general, the model which resulted in the best figures of merit (R_1 and wR_2), the lowest residual density, the lowest correlations between the refined parameters and the physically most meaningful multipole-parameters (monopole populations, κ, κ`) was chosen. In our final model a 4s^{0}3d^4 valence configuration of Ti was assumed.

The atomic coordinates and thermal displacement parameters of all non-hydrogen atoms were optimized along with all multipolar parameters using all data with $\sin\theta/\lambda$ < 1.17 Å^{-1}. During multipolar refinements, the hydrogen positions were restrained with fixed C-H bond distances [r(C-H) = 1.10 Å for hydrogen atoms bonded to sp^3 hybridized carbons atoms; r(C-H) = 1.08 Å for hydrogen atoms bonded to sp^2 hybridized carbon atoms], and their isotropic thermal parameters were freely refined. Only for the hydrogen atoms attached to C(11) the isotropic displacement parameters were related according to U_{iso}(H) = 1.5×U_{eq}(C)], due to anharmonic effects (see below). The positional parameters of the bridging hydrogen atom H(11) was freely refined, and its isotropic thermal parameter was refined during the multipole refinement.

To reduce the number of independently populated multipole parameters a chemical constrained model was employed. The multipole parameters for the carbon atoms C(1-5) and C(6-10) (See Fig. S2 for the definition of the atom labels) and their respective hydrogen atoms in the two Cp rings were constrained to be to same. Due to the tilt of the Cp rings, no strict fivefold symmetry was assumed. Additionally, it was assumed, that the Ti atom lies on a mirror plane, spanned by the P and Si atoms. Furthermore, for all Me groups attached to the phosphorous atom, as well as for the Me group bound to the silicon atom, a local C_{3v} pseudo symmetry was im-

posed. For a definition of the local coordinate systems employed see Supporting Information S2.

In addition, after a multipole model had been applied for all atoms, the thermal motion of the Ti, Si, P atom and both Cl atoms were described by an anharmonic model, using the Gram-Charlier expansion[45] up to the fourth order. The methyl group around C(11), attached to the silicon atom, was also described by an anharmonic model up to the third order. First, all multipolar parameters were kept fix, and only the positional and thermal parameters of these atoms were refined, to avoid correlation between multipole- and anharmonic thermal parameters. In the next step both multipolar parameters as well as all thermal displacement parameters (also anharmonic parameters) were refined simultaneously. The validity of the thermal displacement parameters was carefully checked for negative probability density regions using the XDPDF routine. For Ti(1), Si(1), P(1), and Cl(2), no negative region was found in an atom centered cube with 1.6 Å edge length. For C(11) and Cl(1), minute negative regions were found, however 99.999% and 99.985% of the integrated probability density were positive, justifying the validity of anharmonic motion.

Individual radial scaling parameters (κ) were adopted for all chemically non-equivalent atoms of the molecule (8 in total) to adjust the spherical atomic density contributions. The κ value for the hydrogen atoms was kept fixed at the default value of 1.20 at all times. In addition, a total of 6 radial scaling parameters (κ') were freely refined, while κ' was left at the value of 1.10 for all chlorine atoms and at the value of 1.20 for all hydrogen atoms. The κ-parameter for the bridging hydrogen was freely refined, while its κ'-parameter was kept fixed at 1.0. The total charge of the asymmetric unit was constrained to zero during all refinements.

The final agreement factors were R_1 = 1.42% and wR_2 = 2.69% for 20473 reflections ($F_o > 3\sigma(F_o)$, $\sin(\theta/\lambda)_{max}$ = 1.17 Å^{-1}) and 647 parameters (N_{ref} / N_{var} = 31.6). The final multipole population parameters, fractional coordinates, bond distances and angles are shown in the Supporting Information S4 – S5. The residual electron density distribution was almost featureless with the minimum and maximum values of -0.187/0.262 e/Å^3 throughout the unit cell using a 0.025Å grid using the XDFFT routine ($\sin(\theta/\lambda)$ < 1.00 Å^{-1}). A residual density map in the Ti-Si-H plane is shown in Supporting Information S3a.

All refinements were carried out with the full-matrix least-square program XDLSM of the XD2006 suite of programs, the quantity minimized was $\varepsilon = \Sigma w_1(|F_o| - k|F_c|)^2$, where k is a scale factor, based on 20473 reflections with $F_o > 3\sigma(F_o)$. Weights were taken as $w_1 = 1/\sigma^2(F_o)$ and $w_2 = 1/\sigma^2(F_o^2)$. For sufficient convergence, the spherical κ-parameters for Ti(1) and C(11) had to be fixed. Convergence was assumed when a maximal shift/esd < 10^{-9} was achieved. For the topological analysis, critical points of the electron density were searched by using the XDPROP module of the XD2006 suite of programs, which was also used to calculate the bond paths. Properties of $\rho(\mathbf{r})$ and $\nabla^2\rho(\mathbf{r})$ were calculated after transformation of the local axis system into a global system.

Hirshfeld's rigid bond test[46] as implemented in the module XDLSM of the XD2006 suite of programs was applied to the atomic displacement parameters obtained from the refinements. The difference between mean-square amplitudes for all bonds is within the limit of 1.0•10^{-3}Å^{-2}, except for one P-C bond and one Si-C bond in the where the phosphorous and carbon atom are affected by anharmonic motion, respectively. Also most of the bonds of the Cp-rings to the titanium atom do not fulfil these tests. For a detailed listing of the DMSDA values, see Supporting Information S1.

CCDC 1543832 contains the supplementary crystallographic data for this paper. These data can be obtained free of charge from The Cambridge Crystallographic Data Centre via www.ccdc.cam.ac.uk/data_request/cif.

High pressure (HP) single crystal diffraction. The high pressure (HP) single crystal diffraction experiments were carried out with a Merrill-Bassett type diamond anvil cell (DAC) equipped with conical Boehler type diamond anvils (culet diameter: 0.6 mm).[47,48] In total three single crystals (SC) with different dimensions (SC1: 180 × 170 × 80 μm^3; SC2: 170 × 120 × 70 μm^3; SC3: 120 × 75 × 45 μm^3) were successively measured and only one single crystal was loaded into the DAC for each experiment. The first measurement was interrupted by a partial damage of the first single crystal (SC1) and the second measurement on SC2 was stopped due to the complete destruction of the single crystal at approximately 3.6(1) GPa. In both cases the crystals were bridged between the two mutually approaching diamond anvils. Due to the moisture sensitivity of compound **8c** all crystals were placed into a pre-indented stainless steel gasket inside an Ar-glove box and surrounded by 1:1 volume mixture of iso:n-pentane, which served as pressure-transmitting medium (hydrostatic limit: P = 7 GPa).[49] The pressure was determined by applying the ruby fluorescence method.[50] All in-house measurements were conducted with Bruker SMART-APEX diffractometer equipped with a D8 goniometer and a mirror-focused Ag K_α X-ray source (λ = 0.56087 Å). Additional single-crystal high pressure diffraction experiments were performed at the synchrotron X04SA Material Science-beamline of the Paul Scherrer Institute, Switzerland.[51] In this case a monochromatic wavelength of 0.49726 Å was applied, which had been calibrated to the lattice parameters of a NIST SRM 660a LaB_6 standard. The DAC was mounted onto a Huber Eulerian Cradle 511 which has been connected to the ω circle of the original powder beamline and allowed the rotation of the DAC along the beam.[52] The scattered radiation was collected with a Pilatus 6M detector. For both diffractometer types the collected frames were imported into the CrysAlis^{Pro} software for data reduction including an empirical absorption correction with SCALE3 ABSPACK.[53] The crys-

tal structures at various pressure points were solved by SHELXS and refined by SHELXL.[42] The data and refinement results can be found in the supplementary crystallographic data CCDC 1543404-1543412. These data can be obtained free of charge from The Cambridge Crystallographic Data Centre via www.ccdc.cam.ac.uk/data_request/cif. Detailed information concerning the HP single diffraction experiments and pressure dependency of **8c** are given in the Supporting Information.

ASSOCIATED CONTENT

Supporting Information. Details and tables of the charge density refinement of **8c**; theoretical Laplacian maps of **1-7**, **8c**; details and tables of the high pressure single crystal diffraction study of **8c** (PDF)

The Supporting Information is available free of charge via the Internet at http://pubs.acs.org.

AUTHOR INFORMATION

Corresponding Author

*wolfgang.scherer@physik.uni-augsburg.de

ACKNOWLEDGEMENTS

This work was supported by the DFG (SPP1178) project number SCHE478/9-3. J.E.B.-L. acknowledges DGSCA, UNAM, for supercomputer time via project SC15-1-IR-66.

REFERENCES

(1) a) Corey, J. Y.; Braddock-Wilking, J. *Chem. Rev.*, **1999**, *99*, 175-292; b) Corey, J. Y. *Chem. Rev.* **2011**, *111*, 863-1071; c) Corey, J. Y. *Chem. Rev.* **2016**, *116*, 11291–11435.

(2) a) Matthews, S. L.; Pons, V.; Heinekey, D. M. *Inorg. Chem.* **2006**, *45*, 6453-6459; b) Krentz, R.; Pomeroy, R. *Inorg. Chem.* **1985**, *24*, 2976-2980.

(3) a) Schubert, U. *Adv. Organomet. Chem.* **1990**, *30*, 151-187; b) Crabtree, R. H. *Angew. Chem., Int. Ed.* **1993**, *32*, 789–805; c) Schneider, J. J. *Angew. Chem., Int. Ed.* **1996**, *35*, 1068–1075; d) Lin, Z. *Chem. Soc. Rev*. **2002**, *31*, 239–245; e) Nikonov, G. I. *Adv. Organomet. Chem*. **2005**, *53*, 217–309; f) Scherer, W.; Eickerling, G.; Tafipolsky, M.; McGrady, G. S.; Sirsch, P.; Chatterton, N. P. *Chem. Commun.* **2006**, *28*, 2986–2988; g) Lachaize, S.; Sabo-Etienne, S. *Eur. J. Inorg. Chem.* **2006**, 2115-2127; h) McGrady, G. S.; Sirsch, P.; Chatterton, N. P.; Ostermann, A.; Gatti, C.; Altmannshofer, S.; Herz, V.; Eickerling, G.; Scherer, W. *Inorg. Chem.* **2009**, *48*, 1588–1598; i) Hauf, C.; Barquera-Lozada, J. E.; Meixner, P.; Eickerling, G.; Altmannshofer, S.; Stalke, D.; Zell, T.; Schmidt, D.; Radius, U.; Scherer, W. *Z. Anorg. Allg. Chem.* **2013**, *639*, 1996-2004; j) Stahl, T.; Hrobárik, P.; Königs, C. D. F.; Ohki, Y.; Tatsumi, K.; Kemper, S.; Kaupp, M.; Klare, H. F. T.; Oestreich, M. *Chem. Sci.* **2015**, *6*, 4324-4334; k) Fan, M.-F.; Lin, Z. *Organometallics,* **1998**, *17*, 1092-1100; l) Komuro, T.; Okowara, S.; Furuyama, K.; Tobita, H. *Chem. Lett.* **2012**, *41*, 774-776.

(4) a) Schubert, U.; Scholz, G.; Müller, J.; Ackermann, K.; Wörle, B.; Stansfield, R. *J. Organomet. Chem.* **1986**, *306*, 303-326; b) Schubert, U.; Ackermann, K.; Wörle, B. *J. Am. Chem. Soc.*, **1982**, *104*, 7378-7380; c) Spaltenstein, E.; Palma, P.; Kreutzer, K. A.; Willoughby, C. A.; Davis, W. M.; Buchwald, S. L. *J. Am. Chem. Soc.* **1994**, *116*, 10308–10309, d) Zell, T.; Schaub, T.; Radacki, K.; Radius, U. *Dalton Trans.* **2011**, *40*, 1852-1854.

(5) Scherer, W.; Meixner, P.;Batke, K.; Barquera-Lozada, J. E.; Ruhland, K.; Fischer, A.; Eickerling, G.; Eichele, K. *Angew. Chem., Int. Ed.* **2016**, *55*, 11673-11677.

(6) Scherer, W.; Meixner, P.; Barquera-Lozada, J. E.; Hauf, C.; Obenhuber, A.; Brück, A.; Wolstenholme, D. J.; Ruhland, K.; Leusser, D.; Stalke, D. *Angew. Chem. Int. Ed.* **2013**, *52*, 6092-6096.

(7) a) Dewar, M. J. S. *Bull. Soc. Chim. Fr.*, **1951**, *18*, C71-C79; for charge density based DCD descriptors, see b) Pidun, U.; Frenking, G. *Organometallics* **1995**, *14*, 5325-5336; c) Macchi, P.; Proserpio, D. M.; Sironi, A. *J. Am. Chem. Soc.* **1998**, *120*, 1447–1455; d) Uddin, J.; Dapprich S.; Frenking, G. *Organometallics*, **1999**, *18*, 457-465; e) Scherer, W.; Eickerling, G.; Shorokhov, D.; Gullo, E.; McGrady, G. S.; Sirsch, P. *New J. Chem.* **2006**, *30*, 309–312.

(8) This local coordinate system was originally chosen by D. Lichtenberger to illustrate the optimal overlap between the acceptor orbital σ^*(Si-H) and the metal-based d_{yz} orbital in Schubert-type silane complexes such as **2** and **3**. See, Lichtenberger, D. L. *Organometallics* **2003**, *22*, 1599-1602.

(9) a) Crabtree and Hamilton (CH) proposed in a case study of $CpMn(CO)_2HFSiPh_2$ that the "more electronegative the substituent at Si, the greater the Si character of the corresponding σ^* orbital". In their qualitative MO description the authors assumed that the sp^x-hybridized lobe at the silicon atoms in the σ^* orbital points to the bridging hydrogen atom. As a consequence, CH concluded that "the σ^* orbital will have greater Si character and therefore overlap better with the M-H σ bond, the more electronegative the substituent". However, as illustrated by Figure 3a,b the sp^x-hybridized lobe at the silicon atom in the $\sigma^*(H_{br}–Si–X_t)$ frontier orbital points usually to the metal fragment and rather controls the strength of the M-Si bond. See, Crabtree, R. H.; Hamilton, D. G. *Adv. Organomet. Chem.* **1988**, *28*, 299–338; b) This rehybridization effect has been discussed earlier in transition metal hydrosilane complexes and was interpreted as a signature and consequence of Bent's rule. See for example: Nikonov, G. I.; Kuzmina, L. G.; Vyboishchikov, S. F.; Lemenovskii, D. A.; Howard, J. A. K. *Chem. Eur. J.* **1999**, *5*, 2947-2964. The role of the hybridization of the silicon atom will be discussed in more detail in the subsequent NMR Section of this contribution; c) The shortening of M-Si bonds with increasing number of halogen ligands has been already described in 1977 by Cowie *et al.* and explained by a "shrinkage of the silicon orbital by the more electronegative substituents". In case of complexes **4** and **5** the shrinkage of the $\sigma^*(H_{br}–Si–X_t)$ frontier orbital of the respective free ligands can be estimated by comparing the maximal distance between the iso-contour line at 0.01 a.u. and the silicon center (Figure 3a,b). In this case the LUMO of the SiH_2ClPh ligand is contracted by 3.3% relative to the LUMO of SiH_2ClPh. See, Cowie, M.; Bennet, M. J. *Inorg. Chem.* **1977**, *9*, 2325-2329.

(10) a) Ignatov, S. K.; Rees, N. H.; Tyrrell, B. R.; Dubberley, S. R.; Razuvaev, A. G.; Mountford, P.; Nikonov, G. I. *Chem. Eur. J.* **2004**, *10*, 4991-4999; b) Dubberley, S. R.; Ignatov, S. K.; Rees, N. H.; Razuvaev, A. G.; Mountford, P.; Nikonov, G. I. *J. Am. Chem. Soc.* **2003**, *125*, 642-643; c) Bakhmutov, V. I.; Howard, J. A. K.; Keen, D. A.; Kuzmina, L. G.; Leech, M. A.; Nikonov, G. I.; Vorontsov, E. V.; Wilson, C. C. *J. Chem. Soc., Dalton Trans.* **2000**, 1631–1635.

(11) a) Bader, R. F. W.; Matta, C. F.; Cortés-Guzmán, F. *Organometallics* **2004**, *23*, 6253-6263; for a definition of topological bond catastrophe scenarios, see b) Bader, R. F. W.; Tal, Y.; Anderson, S. G.; Nguyen-Dang, T. T. *Isr. J. Chem.* **1980**, *19*, 8-29; c) Tal, Y.; Bader, R. F. W.; Nguyen-Dang, T. T.; Ojha, M.; Anderson, S. G. *J. Chem. Phys.* **1981**, *74*, 5162-5167; for a discussion of bond catastrophe scenarios in organometallic metal-

lacycles, see for example: d) Scherer, W.; Hieringer, W.; Spiegler, M.; Sirsch, P.; McGrady, G. S.; Downs, A. J.; Haaland, A.; Pedersen, B. *Chem. Commun.* **1998**, 2471– 2472, e) Scherer, W.; McGrady, G. S. *Angew. Chem., Int. Ed.* **2004**, *43*, 1782–1806; f) Scherer, W.; Herz, V.; Hauf, C. *Struct. Bond.* **2012**, *146*, 159–207.

(12) Smith, E. E.; Du, G.; Fanwick, P. E.; Abu-Omar, M. M. *Organometallics* **2010**, *29*, 6527–6533.

(13) Holland, P. L.; Smith, M. E.; Andersen, R. A.; Bergman, R. G. *J. Am. Chem. Soc.* **1997**, *119*, 12815–12823.

(14) a) Johnson, E.; Keinan, S.; Mori-Sánchez, P.; Contreras-García, J.; Cohen, A.; Yang, W. *J. Am. Chem. Soc.* **2010**, *132*, 6498–6506; b) Otero-de-la-Roza, A.; Johnsona, E. R.; Contreras-García, J. *Phys. Chem. Chem. Phys.* **2012**, **14**, 12165–12172; c) Jabłoński, M. *J. Phys. Chem. A,* **2016**, *120*, 4211-4222.

(15) Hansen, N. K.; Coppens, P. *Acta Cryst.* **1978**, *A34*, 909-921.

(16) Colomer, E.; Corriu, R. J. P.; Marzin, C.; Vioux, A. *Inorg. Chem.* **1982**, *21*, 368-373.

(17) Schraml, J.; Bellama J. M. In Determination of Organic Structures by Physical Methods; Nachod, F. C.; Zuckerman, J. J.; Randall, E. W., Eds; Academic Press: New York, 1976; Vol. 6, pp. 203-269.

(18) Ramsey, N. F. *Phys. Rev.* **1953**, *91*, 303-307.

(19) Pioneering NMR calculation of *J*(Si,H) in case of complex **7** yielded couplings of +16 Hz. See ref 8 for further details and the following references for recent theoretical NMR studies of non-classical hydrosilane complexes: a) Horbatenko, Y.; Vyboishchikov, S. F. *Organometallics,* **2013**, *32*, 514-526; b) Horbatenko, Y.; Vyboishchikov, S. F. *ChemPlusChem,* **2013**, *78*, 1073-1081.

(20) Keeler, J. In Understanding NMR Spectroscopy; John Wiley & Sons, 2010, p. 334.

(21) Weinhold, F.; Landis, C. R. *Chem. Educ. Res. Pract. Eur.* **2001**, *2*, 91-104.

(22) a) Muller, N.; Pritchard, D. E. *J. Chem. Phys.* 1959, **31**, 1471-1476; b) Muller, N.; Pritchard, D. E. *J. Chem. Phys.* 1959, **31**, 768-771.

(23) Bent, H. A. *Chem. Rev.* **1961**, *61*, 275-311.

(24) Ebsworth, E. A. V.; Turner, J. J. *J. Chem. Phys.* **1962**, *36*, 2628-2634.

(25) Schraml and Bellama (ref 17) also proposed that an increasing number of electron withdrawing ligands causes an increasing deshielding of the proton. Accordingly, the effective nuclear charge seen by the s-electron of the hydrogen atom also increases with increasing substitution degree n. Consequently, the *J* constants increase with larger *n* values.

(26) a) Autschbach, J.; Ziegler, T. *J. Chem. Phys.* **2000**, *113*, 936-947; b) Autschbach, J.; Ziegler, T. *J. Chem. Phys.* **2000**, *113*, 9410-9418.

(27) van Lenthe, E.; Baerends, E. J.; Snijders, J. G. *J. Chem. Phys.* **1993**, *99*, 4597-4610.

(28) We note that also the charge density at the Si-H BCPs remains rather constant: 0.497 eÅ^{-3} in **8a** (*n*=0); 0.508 eÅ^{-3} Å in **8b** (*n*=1); 0.520 eÅ^{-3} in **8c**, (*n*=2) and 0.513 eÅ^{-3} in **8d**, (*n*=3).

(29) An earlier NMR study by Ignatov et al. (ref 10a) determined negative *J*(Si,H) signs in case of $Cp_2Ti(PMe_3)HSiMeCl_2$ (**8c**) and $Cp_2Ti(PMe_3)HSiCl_3$ (**8d**;) in contrast to our theoretical analysis (Figure 4 and 9 and Table 1). These results were earlier taken as evidence for the presence of pronounced interligand-hypervalent interactions (IHI) in these type of complexes. This effect is defined in terms of a hypervalent electron donation from a σ(*M*-H) orbital into an antibonding σ*(Si-*X*) orbital of a metal coordinating silane ligand. However, recent experimental and theoretical NMR studies (ref 5) suggest that these results rest upon an erroneous sign assignment. In line with the theoretical and experimental charge density studies presented in this study and ref 5 no evidence could be found for the presence/relevance of a significant IHI in complexes **8a-d**.

(30) In the experimental NMR study by Dubberley et al. (ref 10b) the magnitudes of the *J*(Si,H) values were specified for **10b** (33 Hz), **10c** (40 Hz) and **10d** (50 Hz). Solely, in case of complex **10e** the sign of the *J*(Si,H) couplings was experimentally derived and was positive (+14 Hz) in line with our theoretical study (+ 25 Hz).

(31) Kool, L. B.; Rausch, M. D.; Alt, H. G.; Herberhold, M.; Honold, B.; Thewalt, U. *J. Organomet. Chem.* **1987**, *320*, 37–45.

(32) a) te Velde, G.; Bickelhaupt, F. M.; van Gisbergen, S. J. A.; Fonseca Guerra, C.; Baerends, E. J.; Snijders, J. G.; Ziegler, T. *J. Comput. Chem.* **2001**, *22*, 931-967; b) Fonseca Guerra, C.; Snijders, J. G.; te Velde, G.; Baerends, E. J. *Theor. Chem. Acc.* **1998**, *99*, 391-403; c) *ADF2014*; SCM, Theoretical Chemistry, Vrije Universiteit: Amsterdam, The Netherlands, http://www.scm.com.

(33) a) Ernzerhof, M.; Scuseria, G. *J. Chem. Phys.* **1999**, *110*, 5029-5036; b) Adamo, C.; Barone, V. *J. Chem. Phys.* **1999**, *110*, 6158-6170.

(34) van Lenthe, E.; Baerends, E. J. *J. Comput. Chem.* **2003**, *24*, 1142-1156.

(35) a) Chang, Ch.; Pelissier, M. Ph. Durand, *Phys. Scr.* **1986**, *34*, 394-404; b) van Lenthe, E.; Baerends, E. J.; Snijders, J. G. *J. Chem. Phys.,* **1993**, *99*, 4597-4610; c) van Lenthe, E.; Baerends, E. J.; Snijders, J. G. *J. Chem. Phys.* **1994**, *101*, 9783-9792; d) van Lenthe, E.; Ehlers, A. E.; Baerends, E. J. *J. Chem. Phys.* **1999**, *110*, 8943-8953.

(36) Autschbach, J. *J. Chem. Phys.* **2008**, *129*, 094105.

(37) a) Bader, R. F. W. In Atoms in Molecules: A Quantum Theory (International Series of Monographs on Chemistry), Oxford University Press, **1994**; b) Rodríguez, J. I. *J. Comput. Chem.* **2013**, 34, 681-686.

(38) Kohout, M. *Program DGrid*, v4.6; Radebeul, **2011**.

(39) A. Volkov, T. Koritsanszky, M. Chodkiewicz, H. F. King *J. Comput. Chem*. **2008**, *30*, 1379–1391.

(40) Bruker AXS Inc., *SAINT*, v 7.68 A; Madison (WI), USA, **2008**.

(41) Sheldrick; G. M., *SADABS*, v 2008/2; Göttingen, 2008.

(42) a) Sheldrick, G. M. *SHELXL-97*, Program for Crystal Structure Refinement; University of Göttingen, Germany, 1997; b) Sheldrick, G. M. *Acta Crystallogr. Sect. A* **2008**, *64*, 112–122; c) Sheldrick, G. M. *Acta Crystallogr. Sect. C* **2015**, *71*, 3–8.

(43) Stewart, R. F. *Acta Crystallogr.* **1976**, *A32,* 565-574.

(44) Volkov, A.; Macchi, P.; Farrugia, L. J.; Gatti, C.; Mallinson, P.; Richter, T.; Koritsanszky, T. *XD2006 (version 5.42) - a computer program for multipole refinement, topological analysis of charge densities and evaluation of intermolecular energies from experimental or theoretical structure factors*; 2006.

(45) Johnson, C. K.; Levy, H. A. International Tables for X-Ray Crystallography; Kynoch Press: Birmingham, 1974, Vol. IV, pp. 311-336.

(46) Hirschfeld, F. Acta Crystallogr. Sect. A **1976**, *32*, 239-244.

(47) a) Merrill, L.; Bassett, W. A. *Rev. Sci. Instrum.* **1974**, *45*, 290–294; b) Boehler, R.; De Hantsetters, K. *High Press. Res.* **2004**, *24*, 391–396.

(48) Moggach, S. A.; Allan, D. R.; Parsons, S.; Warren, J. E. *J. Appl. Crystallogr.* **2008**, *41*, 249–251.

(49) a) Piermarini, G. J.; Block, S.; Barnett, J. D. *J. Appl. Phys.* **1973**, *44*, 5377–5382; b) Klotz, S.; Chervin, J.-C.; Munsch, P.; Marchand, G. L. *J. Phys. Appl. Phys.* **2009**, *42*, 075413.

(50) Piermarini, G. J.; Block, S.; Barnett, J. D.; Forman, R. A. *J. Appl. Phys.* **1975**, *46*, 2774–2780.

(51) Willmott, P. R.; Meister, D.; Leake, S. J.; Lange, M.; Bergamaschi, A.; Böge, M.; Calvi, M.; Cancellieri, C.; Casati, N.; Cervellino, A. et al. *J. Synchrotron Radiat.* **2013**, *20*, 667–682.

(52) Fisch, M.; Lanza, A.; Macchi, P.; Casati, N. *J. Appl. Crystallogr.* **2015**, *48*, 1956–1963.

(53) a) Oxford Diffraction Ltd., *CrysAlisPro*, V 1.171.37.33; Yarnton, Oxfordshire, UK, **2014**; b) Rigaku OD, *CrysAlisPro*, V 1.171.38.43; Yarnton, Oxfordshire, UK, **2015**.